

University of Nevada, Reno

Study of Single Wires and X-pinchs as X-ray Sources at peak current of 0.9-1.6 MA

A thesis submitted in partial fulfillment of the requirements
for the degree of Master of Science in Physics

By Steven F. Keim

Dr. Victor L. Kantsyrev/Thesis Advisor

December, 2013

© Steven F. Keim 2013
All Rights Reserved



University of Nevada, Reno
Statewide • Worldwide

THE GRADUATE SCHOOL

We recommend that the thesis
prepared under our supervision by

STEVEN F KEIM

entitled

Study of Single Wires and X-pinchs as X-ray Sources at 0.9-1.6 MA

be accepted in partial fulfillment of the
requirements for the degree of

MASTER OF SCIENCE

Victor Kantsyrev, Dr. Sci, Ph.D., Advisor

Alla Safronova, Ph.D., Committee Member

Michael Crognale, Ph.D., Graduate School Representative

Marsha H. Read, Ph. D., Dean, Graduate School

December, 2013

Abstract

Z-pinches are an efficient means of generating high energy density plasmas for studies related to radiation physics, inertial confinement fusion, and astrophysics. This thesis focuses on the study of single wire (SW) Z-pinches and X-pinches at the UNR Zebra generator with respective currents of 0.9 MA and 1.6 MA. SW loads are interesting because of their relative simplicity. They can be used to analyze aspects of Z-pinches that are not visible in multi-wire arrangements. X-pinch dynamics are unique when compared to other load types. They have been studied in detail on Zebra and other facilities in the past at currents ranging from 0.1-1 MA. In this thesis, X-pinches are studied at higher currents as a possible point-like source for X-ray wave-front splitting interferometry. Comparison with previous research done on X-pinches at 0.9 MA is made. Wire materials used for these studies were stainless steel 304 (primarily iron, $Z=26$), copper ($Z=29$), and silver ($Z=47$). The diagnostic suite includes an array of fast, filtered X-ray diodes, bolometers, time-integrated and time-gated pinhole cameras and spectrometers, and laser shadowgraphy. For the first time on Zebra, a wave-front splitting interferometer was fielded to study possible applications of X-pinch loads and laser plasma sources for X-ray holography on university-scale generators.

Acknowledgements

I am extremely grateful for the support of my advisor, Dr. Victor Kantsyrev. He has guided me, challenged me, and shared his expertise innumerable times, and each time I learned something new. His experience in X-ray physics has been indispensable in my studies. Without his guidance and support, none of this would have been possible.

I would like to thank Dr. Alla Safronova, as well, for hiring me as an undergraduate researcher in her group. It was the experience I needed to prepare myself for my current studies. She was always very straightforward in her advice, and always made sure to tell it how it is, even if that wasn't necessarily how I wanted it to be. It was by her guidance that I began supplementing my biology background with higher level math and physics classes. If I hadn't taken those classes as an undergraduate, I wouldn't have had the option to enter the physics graduate program when I did.

I would like to thank Dr. Crognale for taking the time to be a member of my committee, as well as the time he's spent as one of my go-to recommenders in my application process. More than that, I would like to thank him for his work as instructor in the electrophysiology lab and psychophysiology courses I took in the psychology department. Though I already had an interest in electrophysiology, my time in his laboratory as an undergraduate researcher cemented my interest in the brain and visual system.

My coworkers and colleagues have been nothing short of amazing. Michael Weller, Veronica Shlyaptseva, Austin Stafford, Ishor Shrestha, Emil Petkov, Kimberly Schultz and Matt Cooper are some of the best coworkers and confidants I've ever had. Though Ken Williamson and Glenn Osborne have left the group in the last couple rounds of dissertations, they deserve special mention for always having kept things interesting.

Another group that I can't thank enough is our friendly office staff. Particularly Mercy Balderrama, who hired me in 2006 as a systems administrator for the department. If she hadn't, there is no doubt in my mind that the last seven years would have turned out very differently. Having that job gave me the stability I needed in order to be able to focus on my studies and become the nearly passable student I am today. I also want to thank Marvin Wakefield for always putting up with my minor rebellions against student worker regulations and for always having a good story to tell.

The machine shop deserves its own section. Wade Cline and Carl Davidson are awesome. It seemed like every one of the 1500 or so components I had them build was an emergency, and each time they got the job done quickly, many times solving design problems that I hadn't even considered. Without their help, there is simply no way that my load hardware and interferometer could have been constructed as cheaply and within such a short timeframe as it was. Alexey and Oleg at NTF were also critical in last minute adjustments to my device on Zebra. Their speed with modifications saved me from laboratory disasters on several occasions.

I would like to also thank all of the faculty, staff and students at the Leifson physics building as well as the Nevada Terawatt Facility. For lack of room, many people who either guided me or made my day to day experience in the physics department a total pleasure have been left out. Thank you, all of you, for making this experience what it was.

Finally, I want to thank my parents. They've been fantastic parents through the whole business. That's all I could ever ask for.

TABLE OF CONTENTS

List of tables	vi
List of figures	vii
Chapter 1: Introduction	1
1.1 Overview of Z-pinches	1
1.1.1 X-Pinches	1
1.1.2 Single Wires	5
1.2 Laser Plasma Source on Sparky	6
1.3 Interferometry	7
1.3.1 Partially Coherent Interferometry & Wavefront Splitting	10
1.3.2 Interferometry, the water Window and Selection of Materials	12
Chapter 2: Experimental Setup	13
2.1 Overview of the Zebra Pulsed Power Generator	13
2.2 Overview of the Sparky Facility	15
2.3 Overview of Standard Diagnostics on Zebra	17
2.4 Interferometry Diagnostic Overview	20
Chapter 3: Single Wires at 0.9 MA	25
3.1 Experimental Details	25
3.2 Radiation and Specific Shot Parameters	26
3.2.1 Silver Single Wire Loads 2459 & 2460	27
3.2.2 Stainless Steel SW Load 608	33

Chapter 4: X-Pinches at 1-1.6 MA	38
4.1 Experimental Details	38
4.2 Radiation and Specific Shot Parameters	39
4.2.1 Copper X-Pinch Load 3111	39
4.2.2 Stainless Steel X-Pinch Load 3117	43
Chapter 5: X-ray Wavefront Splitting Interferometry Investigations	48
5.1 Nature of the Source	48
5.2 Experiments on Sparky Facility	48
5.3 Experiments on the Zebra Generator	50
5.4 Image Reproduction	52
Chapter 6: Conclusion	55
6.1 X-pinches and Single Wire Loads	55
6.2 Interferometry	56
References	57

List of Tables

Table 2.1. Operational specifications for Zebra operating in “standard mode”.

Table 2.2. Sparky laser specification summary.

Table 3.1. Primary diodes and their respective sensitivities.

Table 3.2. Load and implosion parameters for single wire loads.

Table 3.3. Diagnostically important lines for silver used in this analysis.

Table 3.4. Diagnostically important lines for stainless steel, composed primarily of iron, chromium and nickel.

Table 4.1. Load and implosion parameters for X-pinches with LCM.

Table 4.2. Diagnostically important lines for Cu.

Table 5.1. Summary table of all shots performed on Sparky. Arrows on shots 8, 9, 12, and 13 indicate that one hole was closed.

Table 5.2. Load and implosion parameters for X-pinches with LCM.

List of Figures

Figure 1.1: An example of X-pinch types, wire-twisted and planar loops. The blue arrow indicates current flow direction.

Figure 1.2. From the JQSRT article by Kantsyrev (2006). Proposed stages of X-ray multiburst and electron beam generation in X-pinch. Stages A-D repeat several times, generating multiple X-ray bursts, until the plasma finally collapses in stage E. 1, 2. Initial wire positions with possible generation of hot spots along wires. 3. Narrow plasma neck between anode and cathode parts of the X-pinch. 4. Hot spot in the neck. 5. The direction and location of the first type of electron (shown alongside the neck for clarity). 6. Expanding plasma. 7. The direction and location of the second type of electron beam. 8. The plasma column formed near the end of the current pulse. 9. The direction and location of the third type of electron beam.

Figure 1.3. On the left is an actual laser produced plasma jet on Sparky. On the right is a diagram detailing the “anatomy” of the plasma jet production.

Figure 1.4: Airy disc pattern associated with coherent light passing through a pinhole.

Figure 1.5: An example of a Michelson interferometer. This is a common design for laser interferometry.

Figure 1.6: Wave-front splitting, the basic scheme for Young’s double slit experiment as well as the experimental system used for interferometry in this research. On the right a vertical intensity distribution can be seen similar to that in Figure 1.4.

Figure 2.1. Scaled illustration and power flow schematic for Zebra, including labels for the four main components (Bauer 1997).

Figure 2.2. The Load Current Multiplier (LCM) position relative to the rest of the Zebra pulsed power generator at NTF. Current of 0.9 MA in standard mode and up to 1.7 MA (wire arrays) and 1.9 MA (short circuit) with the LCM. Current rise-time is 100-110 ns. Impedance is 1.9 Ω . Initial stored energy is approximately 150 kJ.

Figure 2.3. Sparky Facility. 1) Laser. 2) Vacuum chamber for the target. 3) Interferometry beamline.

Figure 2.4. Cu slab target with ablation marks.

Figure 2.5. A standard arrangement for diagnostics on Zebra at NTF. Differences from campaign to campaign are typical, dependent on material and spectral range being studied.

Figure 2.6. An idealized scheme for interferometric recording. a) Plasma source, from either Zebra or Sparky. b) Initial constraining pinhole. c) Double aperture unit. d1) Distance between the plasma source and the first pinhole, which primarily affects light intensity. d2) Distance between the first pinhole and the double aperture, which must be calculated based on the

wavelength of light being studied. d3) Distance between the double aperture and the film, which affects the resolution of the fringe patterns in the exposure. e) Film holder.

Figure 2.7. Adjustable film mount unit. In the above figure, from left to right, it is displayed from the front, rear and side. This unit was also used to mount the double aperture, shown in Figure 2.8.

Figure 2.8. Adjustable film mount converted to mount for double aperture.

Figure 2.9. Adjustable mount for initial constraining pinhole. Pinhole shown is 250 μm .

Figure 2.10. Film canister for trials on sparky. a) Film backplate. b) Filter mount. c) Filter mount holder. d) Film securing ring.

Figure 2.11. Final adjustable film mount for trials on Zebra, designed so that the front and back detach independently. The rear compartment is for the film and the front compartment is where the filter is attached. Front, side and rear views are shown from left to right.

Figure 2.12. Compacted version of interferometer for use on Zebra. The entire assembly without the double pinhole unit is shown.

Figure 2.13. Close-up of the film holder and pipe-mount assemblies (left) and the front aperture mount (right).

Figure 3.1. A single wire load (SW) between the anode (top) and cathode (bottom) on Zebra. The thick posts on either side of the array are removed after installation into the load chamber.

Figure 3.2. Signal Data for Zebra shot 2459.

Figure 3.3. Signal data for Zebra shot 2460.

Figure 3.4. Time-gated pinhole (TGPH) images for shot 2459 filtered for $>1\text{keV}$ and $>3\text{keV}$. Time is counted from current start.

Figure 3.5. Time-gated pinhole (TGPH) images for shot 2460 filtered for $>1\text{keV}$ and $>3\text{keV}$. Time is counted from current start.

Figure 3.6. Laser backlighting images from shots 2459 and 2460. Time is counted from current start.

Figure 3.7. A visual and graphical analysis of gradient formed along z-axis in shot 2459.

Figure 3.8. A visual and graphical analysis of gradient formed along z-axis in shot 2460.

Figure 3.9. Signal data for Zebra shot 608.

Figure 3.10. Time-integrated pinhole images for shot 608. It is filtered to show radiation below 4.4\AA on the left and above 10.7\AA on the right. The anode is on top and the cathode at bottom.

Figure 3.11. Time-integrated spectra lineout for shot 608 with a non-LTE kinetic model overlaid. Units for vertical axis are in calibrated relative intensities. Red lines are modeled and blue lines are experimental data.

Figure 4.1. An X-pinch load on Zebra. This particular photo demonstrates that two different wire materials can be used on the top and bottom, in this case Silver and Alumel, respectively.

Figure 4.2. Signal data for Zebra shot 3111.

Figure 4.3. Optical diagnostics for shot 3111. Shown are ICCD (left) and shadowgraphy (middle, right) images at 43ns and 50ns, respectively.

Figure 4.4. Time-gated soft X-ray spectra for shot 3111. Times (from top to bottom) are 50ns, 56ns, 63ns, 69ns, 75ns, and 80ns, counted from current start.

Figure 4.5. Time-integrated spectra lineout for shot 3111 with non-LTE kinetic model overlaid. Units for vertical axis are in calibrated relative intensities. Red is synthetic spectra and blue is experimental.

Figure 4.6. Signal data for Zebra shot 3117.

Figure 4.7. Optical diagnostics for shot 3117. Shown are ICCD (left) and shadowgraphy (middle, right) images at 32ns and 38ns, respectively.

Figure 4.8. Time-gated pinhole images for shot 3117 filtered for $>1\text{keV}$ and $>3\text{keV}$. Time is counted from current start.

Figure 4.9. Time-integrated pinhole images for shot 3117. Image on the left is filtered at $>1\text{keV}$ and image on right is filtered at $>3\text{keV}$.

Figure 4.10. Time-integrated spectra lineout for shot 3117. Temperature and density modeling was inconclusive.

Figure 5.1. Trial 19 on Sparky with two $30\mu\text{m}$ apertures and ~ 1100 exposures. On the right is a magnification of the exposure.

Figure 5.2. Filter transmissions for Al, mylar, and polypropylene and all three combined. Sample mid-z L-shell spectra is included with an expected intensity after filtration.

Figure 5.3. Magnification of area of interest in shot 3119. Exposure width is about 1.4 mm.

Figure 5.4. Reproduction diagram. a) Film with stored image. b) Magnification Lens for expanding image. c) Refocusing Lens. For focusing magnified image on CCD. d1- d3) Distances associated with reproduction scheme. 1 and 2 are arbitrary, whereas 3 is based on degree of magnification.

Figure 5.5. Reproduction of image from trial #19 on Sparky facility. Background produced without film (left) and reproduction of interferometry image (right).

Figure 5.6. Reproduction of interferometry image acquired during Zebra shot 3119. Background produced without film (left) and reproduction of interferometry image (right). An interference pattern is visible on the right half of the right image. Measured distance between fringes was 0.23 mm.

Chapter 1: Introduction

1.1 Overview of Z-pinches

This thesis covers a range of topics related to the study of point-like Z-pinch X-ray sources. One possible application of this type of source is partially coherent X-ray interferometry. This research required the characterization of the X-ray sources and the development of a simple interferometry device designed to demonstrate the possibility of obtaining X-ray interferometric images at a University-scale Z-pinch generator.

The benefit of Z-pinches is that they are one of the best methods for producing extremely bright sources of radiation, ranging from above the visible spectrum all the way to hard x-ray radiation ($>1\text{MeV}$). In the case of Zebra, the pulse-powered z-pinch generator at the Nevada Terawatt Facility (NTF), this radiation is very accessible via a series of ports placed around the discharge chamber. Z-pinch generated plasma is useful for laboratory astrophysics, radiation science, high energy density physics, and inertial confinement fusion (ICF) studies (Bailey, 2002; Lebedev, 2002; Kantsyrev, 2006; Safronova, 2006; Ampleford, 2007).

1.1.1 X-Pinches

X-pinches have been actively investigated since the 1980's after I. Ulshmidt proposed the design in 1982 during his visit to the P.N. Lebedev Institute (Zakharov et al., 1982). An X-pinch load is typically formed by crossing diagonally aligned wires at a center point between the anode and cathode. This can range from an array as simple as two wires crossed over to one as complex as a high-n cylindrical array that has been crossed over into two cone-like structures. X-pinches have been shown as excellent small sources with hot and dense plasma. 1 MA X-pinches generate short duration X-ray bursts in a wide spectral region (Kantsyrev et al., 2003, 2006; Safronova et al., 2003, 2006). In the same studies, they were proven to be excellent X-ray power sources for

polarimetry (Shlyaptseva, 2001), X-ray backlighting and also to produce strong electron beams (Kantsyrev, 2003).

At the Zebra facility, two configurations have been most commonly used. One of these is the twisted wire type and the other is the planar loop. Both types are illustrated in Figure 1.3.

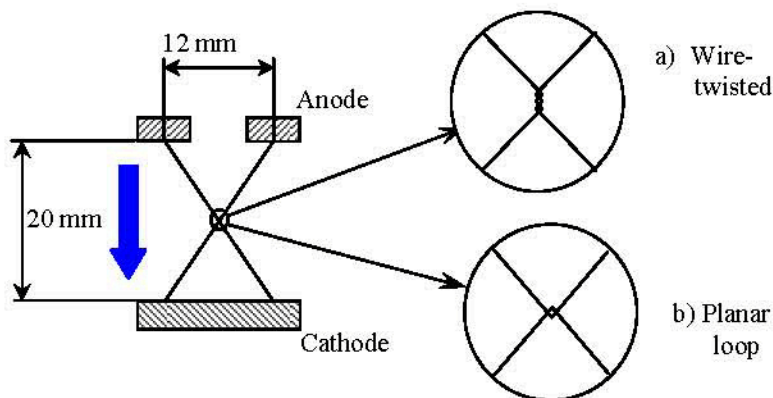


Figure 1.1. An example of X-pinch types, wire-twisted and planar loops. The blue arrow indicates current flow direction.

The twisted-wire X-pinch configuration on the Zebra machine is formed by twisting of the top and the bottom part of the load to an angle approximately $15\text{-}30^\circ$ after wires touch each other. The twisted-wire X-pinch loads are often made of 2 or 4 wires placed in the anode-cathode gap. The planar loop configuration is constructed by passing the top wire through an already formed bottom loop and then suspending the bottom half of the wire load from the top half. As a result top and bottom part of X-pinch remain in the same plane and can be made from different materials. Regardless of construction method, the combined angle between diagonal wires was approximately 62° . Tests on Zebra have shown that the planar loop X-pinch configuration gives a higher X-ray emission yield as well as reasonable reproduction of plasma parameters and output (Fedin, 2004). Taking these properties of the planar loop X-pinch into account, this configuration

was utilized in these studies on Zebra. Wire diameters in planar loop X-pinch configurations ranged from 30 to 170 μm .

In terms of the characterization of their implosions, X-pinch configurations have some unique features that make them valuable for studies requiring point-like sources. Most of the bright spots in X-pinch configurations are localized near the crossing point of the wires, which creates a more easily accessible plasma source for precision diagnostics. In most cases, it is a cluster of bright spots, with more and larger bright spots in the soft X-ray spectrum. In the hard X-ray spectrum, there are less and more compact bright spots. The small size and high intensity of the source at the center of the X-pinch make it attractive for applications in the soft X-ray (Hammer et al., 1990) and hard X-ray (Kantsyrev et al., 2003) wavelength ranges.

The beginning stage of an X-pinch explosion is similar to single wire explosion (Zakharov et al., 1984), which will be covered more directly in the following section on single wire loads. The wire material ablates and ionizes very quickly relative to current rise time, particularly at the central crossover point. Short X-ray bursts from small bright spots can be detected around this contact point as early as 25ns after current start. Though the locations of these bright spots occur within a region of about 1-2mm, the parameters of the source are often variable during the time frame of a shot and certainly between shots. For example, X-pinch experiments (Shelkovenko, et al. 2001; Fedin 2004; Kantsyrev, 2006) demonstrated that the X-ray source size can vary from only a few microns to over a hundred microns, with emission times ranging from a fraction of a nanosecond up to several nanoseconds (Sinars et al., 2001). Due to these properties, accurate measurements of X-pinch parameters require a combination of precise, well-calibrated diagnostics with good spatial, temporal, and spectral resolution.

In the last decade, there has been significantly more interest in X-pinch configurations. X-pinch configurations have now been studied in detail on Zebra at currents of approximately 1MA (Kantsyrev, et al., 2006, Safronova, et al., 2006) and more recently at ~ 1.7 MA. Novel load types designed to

behave like X-pinches are currently being fielded on SATURN at Sandia National Laboratories (Sinars, 2012).

In earlier studies with X-pinches (keV to sub-MA range), Aluminum and Palladium were used. In one such study, the dynamics of 0.2-0.4 MA X-pinch plasma bright spot formation was studied by X-ray backlighting with sub-nanosecond and 2-3 μm spatial resolution as well as time-integrated spectroscopy (Shelkovenko et al., 2001). In this regime, it was shown that X-ray bursts are emitted from the finest necks in the unstable Z-pinch near the original crossing point of the wires. The location of these bright emission points is near the end of the narrowest necks that form in the imploding X-pinch. After imploding at a rate of tens of $\mu\text{m}/\text{ns}$, the plasma at the central bright spot explodes with some of the ions moving hundreds of $\mu\text{m}/\text{ns}$, and a shock wave is launched into the surrounding plasma. Photoconducting detectors (PCD), time-resolved spectroscopy, and X-ray streak radiographs have shown that most X-pinches generate more than one X-ray pulse, especially in the higher energy range.

In the studies at NTF, a wide range of diagnostics were employed. It was found that the approximately 100 ns rise time on Zebra led to quick vaporization and ionization of the wire material and then yielded several short (0.5-10 ns) thermal X-ray bursts in a wide spectral range. In this case, the size of bright spots were anywhere from several to 100 μm , surrounded by cooler plasma up to several millimeters wide (Kantsyrev 2006). In the Kantsyrev study, stages of the multiburst regime were proposed, which shows time dependent irregularities in the plasma production, similar to those found in SWs.

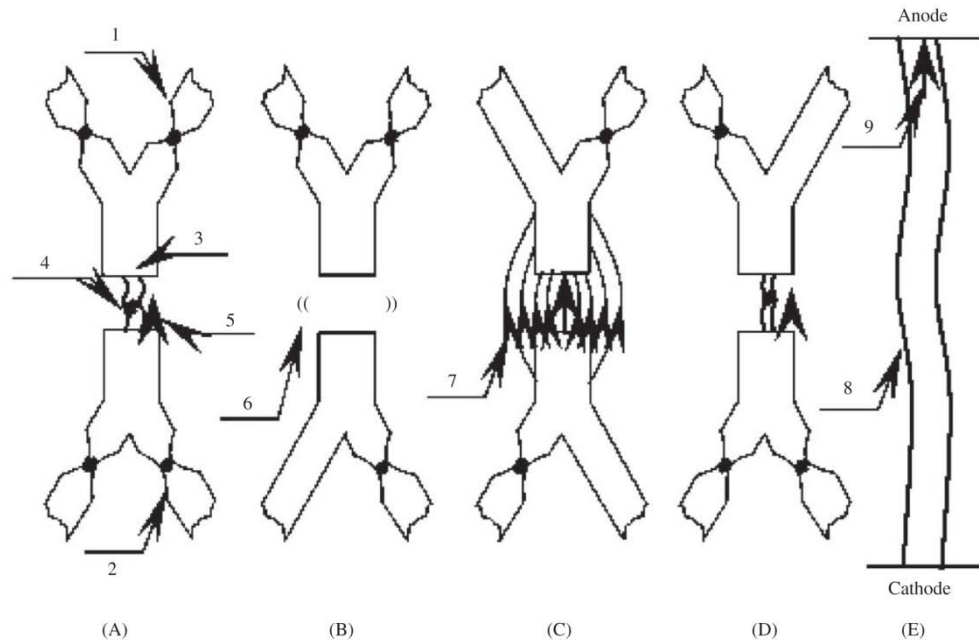


Figure 1.2. From the JQSRT article by Kantsyrev (2006). Proposed stages of X-ray multiburst and electron beam generation in X-pinchs. Stages A-D repeat several times, generating multiple X-ray bursts, until the plasma finally collapses in stage E. 1, 2. Initial wire positions with possible generation of hot spots along wires. 3. Narrow plasma neck between anode and cathode parts of the X-pinch. 4. Hot spot in the neck. 5. The direction and location of the first type of electron (shown alongside the neck for clarity). 6. Expanding plasma. 7. The direction and location of the second type of electron beam. 8. The plasma column formed near the end of the current pulse. 9. The direction and location of the third type of electron beam.

1.1.2 Single Wires

Single wire loads (SWs) are the simplest possible source for pulse generators, consisting of a single wire which is suspended along the z -axis from the anode to cathode. Though the design is straightforward, the characteristics of the pinch are not, due to a multitude of minute irregularities in the material and the subsequent instabilities that occur without a more uniform $\mathbf{j} \times \mathbf{B}$ force. That isn't to say these forces aren't encountered, but if so, they would be smaller and much less effective at stabilizing the pinch. Still, SWs can be used to analyze aspects of Z-pinchs that are not visible in multi-wire arrangements. Specific to SW loads, however, are the mixed dynamics in which both explosive and implusive properties are seen during the shot (Hammer et al., 2001; Esaulov, 2008). This is primarily due to the load material of a single wire

being located along the z-axis, which changes the magnetic properties of the pinch. Previous experiments (Pereira and Davis, 1988) with single-wire Z-pinch loads reveal small localized sources of x-ray radiation (“hot” or “bright” spots) formed at random points along the wire length. Though unpredictable positioning of bright spots in SW experiments makes them more difficult to study, employment of diaphragms in order to constrain the source to something more centralized is possible. Thus, the study of SWs as X-ray sources may yield a new avenue for interferometry investigations like those discussed in this paper.

1.2 Laser Plasma Source on Sparky

The Sparky experimental setup consists of a pulsed laser producing energies of approximately 0.3 Joules per shot with pulse duration of 3 ns. At the focal point of this beam (flux density 10^{13} W/cm²), a target plate consisting of the material is placed. When the laser fires, it ignites the material in the target. This creates a small plasma jet with dimensions of about 0.1-2mm, comparable in size to bright spots found in pinch experiments on Zebra. Because of these properties, Sparky is an excellent test bed for interferometry trials on Zebra. Previous studies of copper on Sparky have shown significant M-shell transitions in the wavelength range of 12 nm to well over 20 nm. Modeling with Spect3D, laser plasma temperature was approximated within a range of 25-90 eV and density was 10^{19} cm⁻³ (Weller, 2012). For interferometry studies, a 158 nm Zirconium filter was used in order to limit the radiation wavelength to below 18 nm. Small apertures were then used to further simulate a coherent x-ray source. In Figure 1.3, an example of a laser produced plasma jet on Sparky can be seen. This demonstrates the point-like source nature of plasmas produced on this system.

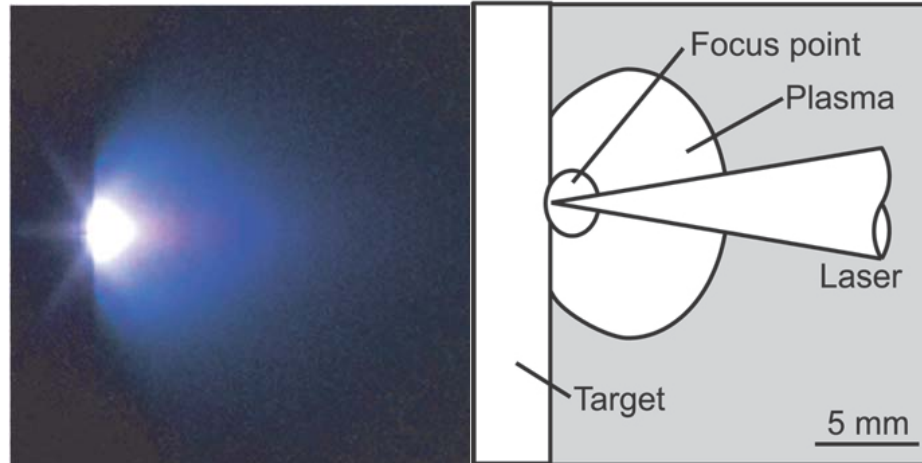


Figure 1.3. On the left is an actual laser produced plasma jet on Sparky. On the right is a diagram detailing the “anatomy” of the plasma jet production.

1.3 Interferometry

Interferometry consists of a number of related techniques in which electromagnetic waves are superimposed. This technique utilizes the electromagnetic interference phenomenon, in which propagating waves interfere constructively or destructively in what is at its core simply a redistribution of energy. For a plane wave, the phase difference is given by

$$\Delta\varphi = \frac{2\pi d}{\lambda} = \frac{2\pi x \sin \theta}{\lambda} \quad (\text{eq. 1.1})$$

The reason this important is that the information that is acquired through the interferometry process comes from differences in phase between the various light sources. Two waves are in phase when

$$\frac{x \sin \theta}{\lambda} = 0, \pm 1, \pm 2, \dots \quad (\text{eq. 1.2})$$

Based on this, it can be quickly seen that the maxima in an interference pattern for plane waves corresponds to

$$d_f = \frac{\lambda}{\sin \theta} \quad (\text{eq. 1.33})$$

where d_f is distance between constructive interference fringe spacing. When dealing with a point source and a constraining circular aperture, this pattern then corresponds to the spatial layout of an airy disc pattern (Figure 1.4).

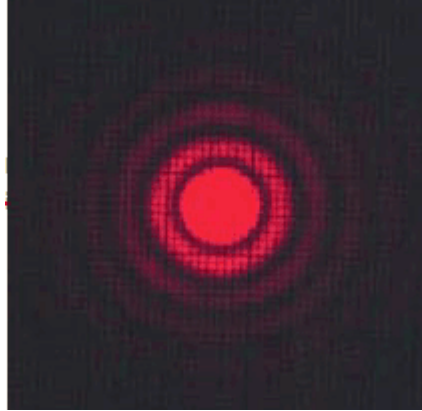


Figure 1.4. Airy disc pattern associated with coherent light passing through a pinhole (Nave, 2012).

In this case, the equation must be modified to take into account the size of the aperture, and values for minima and maxima become constants based around this recalculation. The resulting equation is

$$\sin \theta = \frac{m\lambda}{d_a} \quad (\text{eq. 1.4})$$

with m being replaced with the appropriate values for the order of the fringe pattern one is looking at. The variable d_a represents the diameter of the pinhole being used. This facilitates calculating the interference pattern for a double aperture, where the most direct method for overlapping two such fringes is to calculate their location based on wavelength and distance to the target, then place the aperture appropriately.

What all of this discussion amounts to is the underlying theory behind interferometry techniques. This allows information to be extracted in a more robust manner than basic 2D imaging techniques. There are numerous methods of splitting coherent beams into multiple in-phase sources. Perhaps the most common configuration, and most certainly the earliest known, is the Michelson interferometer (Figure 1.5).

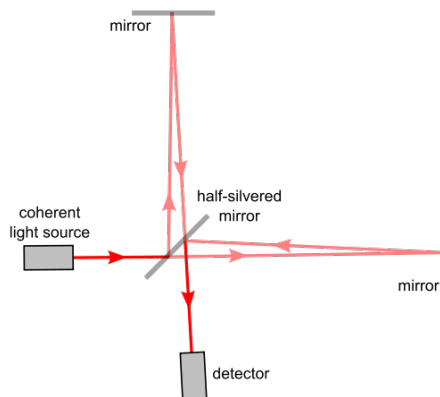


Figure 1.5. An example of a Michelson interferometer. This is a common design for laser interferometry.

The Michelson interferometer is a useful example of coherent interferometry techniques because it demonstrates all of the most important components. First, there must be a coherent light source, typically a laser. Next, the source must be split into two or more beams of matching intensity by a mirror specified to this task at the appropriate wavelength. One of these paths is used as a reference beam, and the other is used as an illumination beam. To keep phase the same, any difference in length must equal a full phase shift, but it is more typical to keep beam paths the same length. Because both beams contain the same source information and are in phase, illuminating an object with one of the beams results in a perturbation in the propagation of the wave. A wavelength should be chosen that can sufficiently penetrate the test object, as light must pass through the object in order to create an interference pattern at the detector. The final portion of the interferometer is the detector, which can be a film substrate or a digital acquisition method. Both beams, one of them altered by the examined object, will illuminate the detector and the

difference between the two beams at that point will give a wealth of information about the object. Data acquired through this method is typically density related and can be used on materials that are in any phase of matter, from solid to plasma. (Nave, 2012)

1.3.1 Partially Coherent Interferometry and Wavefront Splitting

Up to this point, interferometry was discussed with the use of a coherent source. With the advent of lasers as an easily accessible means for coherent light sources in the visible spectrum, interferometry investigations have shifted in favor of this method. However, it is not only possible to use incoherent sources, but in some cases it can be favorable. For instance, there are very few accessible sources of coherent light in the X-ray to hard X-ray portion of the spectrum. Synchrotrons are the primary method of producing coherent X-ray radiation. Synchrotrons work by taking advantage of the phenomenon in which energy emitted when charged particles are accelerated radially. Requiring electromagnets and particle accelerators, these tend to be expensive and inaccessible for university research groups. A possible solution is that at the Zebra facility, high-energy, point sources of radiation are created regularly and by constraining a source through an initial aperture, at which point sufficiently coherent light can theoretically be used to form interferograms.

There are differences in the physics between coherent and partially coherent interferometry, however. In the first case, interference patterns have well defined spatial distributions. In the other case, these interference patterns are less stable, in some cases requiring a statistical average in order for well-defined interference patterns to emerge. Additionally, incoherent interference relies entirely on the first-order spatial correlation of the two fields, so the object information is contained in the joint diffraction of the two fields (Wang, 2011).

In our case, the use of an aperture constrains the source into something point like, so spatial distribution patterns can theoretically occur in one exposure, rather than relying on statistical averages. For partially coherent interferometry, it is valuable to design a system in which temporal coherence, the factor that relates to the constraint on differences in beam path length, can be mostly ignored. Because of this, a technique known as Wavefront splitting interferometry can be employed. Wavefront splitting was one of the first methods developed for proving the interference properties of light in Young's double slit experiment. It employs two slits or apertures at a sufficient distance from the point source (Figure 1.6).

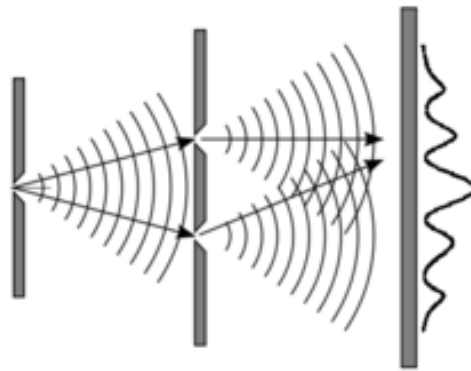


Figure 1.6. Wave-front splitting, the basic scheme for Young's double slit experiment as well as the experimental system used for interferometry in this research. On the right a vertical intensity distribution can be seen similar to that in Figure 1.4.

The wavelength of light used, the distance between the apertures, the size of the apertures themselves, and the distance to the detector or film are all variables that contribute to the resultant interference pattern. Because the apertures are the same distance from the source, path length remains equal between the two and any phase shifts that might occur due to path length differences are negated. At this point, only spatial coherency needs to be controlled, which can be increased by having a bright enough source and constraining it with small enough pinholes. The theory behind a highly adjustable interferometer concept that utilizes these basic principles is discussed below and its specific design and construction is discussed at the end of chapter 2.

1.3.2 Interferometry, the Water Window and Selection of Materials

The experimental design for wave-splitting interferometry on Zebra was devised in such a way that applications to biological imaging could be identified. This first involved consideration of the spectral dimensions of the “water window”, a phenomenon encountered in soft X-ray biological imaging studies. The water window is a wavelength range between approximately 2-5 nm in which water is transparent for light (Mikolajczyk et al., 2010). This allows for efficient imaging of biological samples by utilization of radiation in this spectral region.

For this reason, materials were chosen in these studies that would produce spectra in this range. From previous work on Zebra by Safronova (2006), Cu was shown to be an excellent L-shell radiator at 4.74 nm, so it was chosen. Trials were done with SS 304 and Mo as well, because they are known to radiate well within this regime. Mo, for instance, demonstrates significant L-shell transitions at approximately 4.4 nm. With copper, periods for constructive interference bands were calculated to be 0.62 mm, which should directly control the fringe dimensions and resolution of the final interferometric image. Depending on experimental conditions, the overlapped constructive interference bands can additively be seen in a period of 0.31-0.93 mm with an ideal period of 0.62 mm. Since intensity drops off considerably as the radius of the interference pattern increases, significant deviation from this is expected.

Chapter 2: Experimental Setup

2.1 Overview of the Zebra Pulsed Power Generator

Originally constructed as HDZP-II at Los Alamos National Lab, Zebra is a pulsed power generator at the Nevada Terawatt Facility with a standard current of approximately 1MA (Scudder, 1991; Bauer, 1997). With the Load Current Multiplier installed, current as high as 1.7-1.9 MA can be achieved (Chuvatin, 2010).

Zebra consists of four main sections. The first is the Marx bank generator, which consists of 36 capacitors submerged in oil, charged in parallel, and then discharged in series. Once discharged, the microsecond pulse travels to the second section, a drum-shaped intermediate capacitor. This and the remaining sections are submerged in DI water. The third section is the water transmission line, which is preceded by the gas switch and followed by water switches. This section is constructed so that in conjunction with the intermediate capacitor, the larger microsecond pulse can be compressed into a pulse that reaches max current with an approximately 100 ns rise time. The final section is the load chamber, which although submerged in water, can be accessed from above in order to be accessed for seating experimental loads. This power flow between subunits can be better visualized in Figure 2.1. In Table 2.1, operational parameters of Zebra are summarized.

Generator Inductance	26 nH
Chamber Inductance	30 nH
Impedance	1.9 Ω
Current Max	1.0 MA
Rise Time	100 ns
Marx Energy	150 kJ
Marx Bank Voltage	85 kV

Table 2.1. Operational specifications for Zebra operating in “standard mode”.

An important note on the construction of Zebra is its relatively high line impedance. This is a result of the 0.3 m distance between the anode-cathode gap in the center of the chamber and the chamber walls, which serve as the current return path. Zebra was constructed in this manner purposely in order to make it insensitive to a wide array of load types, but more specifically to implode frozen deuterium fibers (Scudder, 1991).

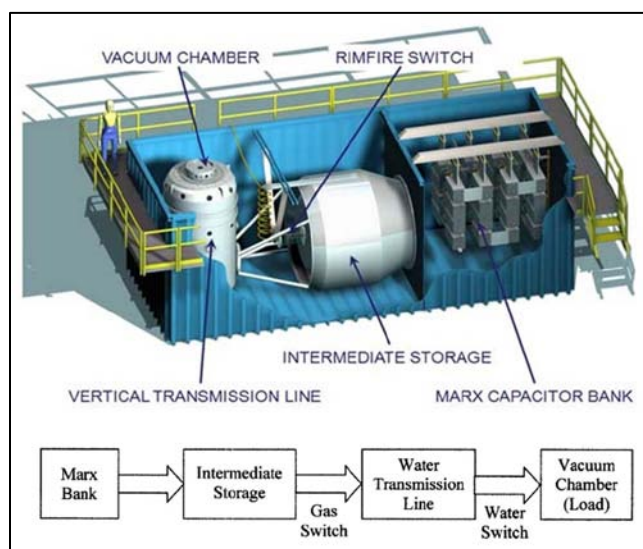


Figure 2.1. Scaled illustration and power flow schematic for Zebra, including labels for the four main components (Bauer, 1997).

An important recent development on Zebra which allowed for the studies in this paper was a significant increase in current. This was made possible by the implementation of a “Load Current Multiplier” (LCM), which effectively doubled the current. The LCM is a modification of the vacuum chamber in which two concentric toroids replace the anode. The current flows into the LCM along the inner surface of the largest electrode, where it then induces an equal and opposite current in the opposing electrode. Both currents are combined to produce a multiple of the original current. In the case of the current LCM unit, the current is doubled, but it is possible to use this method in order to achieve higher multiples (Chuvatin, 2010). Functionally, this uses impedance parameters to improve the energy transfer efficiency. This technique can extend the plasma-load current to as high as 1.9 MA in short circuit shots without a significant modification to the overall Zebra generator structure (Kantsyrev, 2010).

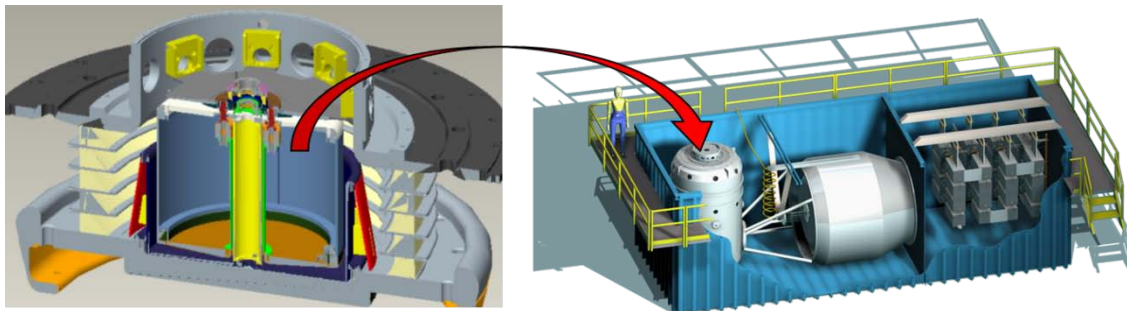


Figure 2.2. The Load Current Multiplier (LCM) position relative to the rest of the Zebra pulsed power generator at NTF. Current of 0.9 MA in standard mode and up to 1.7 MA (wire arrays) and 1.9 MA (short circuit) with the LCM. Current rise-time is 100-110 ns. Impedance is 1.9 Ω . Initial stored energy is approximately 150 kJ.

2.2 Overview of the Sparky Facility

The Sparky facility is operated in two modes. One mode is a pinch generator, whereas the other is as a laser plasma source (Kantsyrev, 2004). For the purposes of this thesis, all references

to the Sparky facility will be in reference to its use as a laser plasma source. The specifications of the laser are summarized in Table 2.2.

Lasing medium	Nd:YAG
Wavelength	1.06 μm
Repetition rate	10 Hz
Pulse duration	3 ns
Pulse energy	0.3 J
Beam Divergence	6×10^{-4} rad
Minimum spot size	20 μm
Maximum flux density on a target	10^{13} W/cm ²

Table 2.2. Sparky laser specification summary.

The electron temperature of plasma produced by Sparky can exceed 200-300 eV and produce radiation above 1500 eV (Fedin, 2005). Above 1000 eV, the effective source size is approximately 2.5 mm and can be used as a point source for testing diagnostics or interferometry studies like those featured in later chapters. However, the energy in this spectral range is approximately 0.03 J and the duration is within the same order of magnitude as the laser pulse. Typically, hundreds of shots are repeated to produce spectra for a given material. During shot repetition, the target is translated in order to avoid cratering. This maintains the target at the optimal focal point, which maintains a relatively consistent flux density (Williamson, 2011). In Figure 2.3, the Sparky experimental system and vacuum chamber are pictured. In Figure 2.4, a copper slab used in the production of M-shell Cu plasmas is shown.

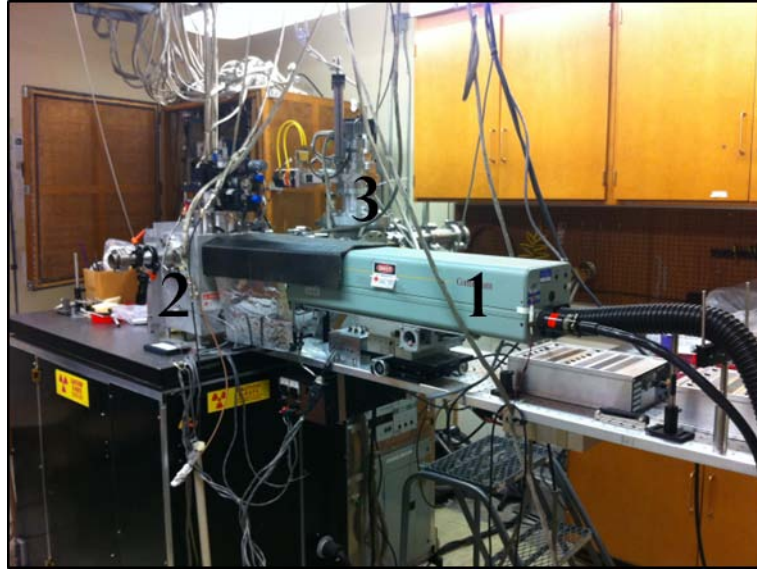


Figure 2.3. Sparky Facility. 1) Laser. 2) Vacuum chamber for the target. 3) Interferometry beamline.

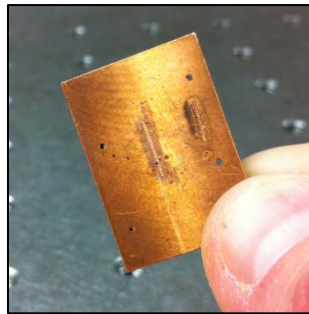


Figure 2.4. Cu slab target with ablation marks.

2.3 Overview of Standard Diagnostics on Zebra

This section will be an overview of diagnostics used primarily on Zebra as per Figure 2.5. The layout changes depending on shot-specific requirements, but overall, diagnostics used stays fairly standardized.

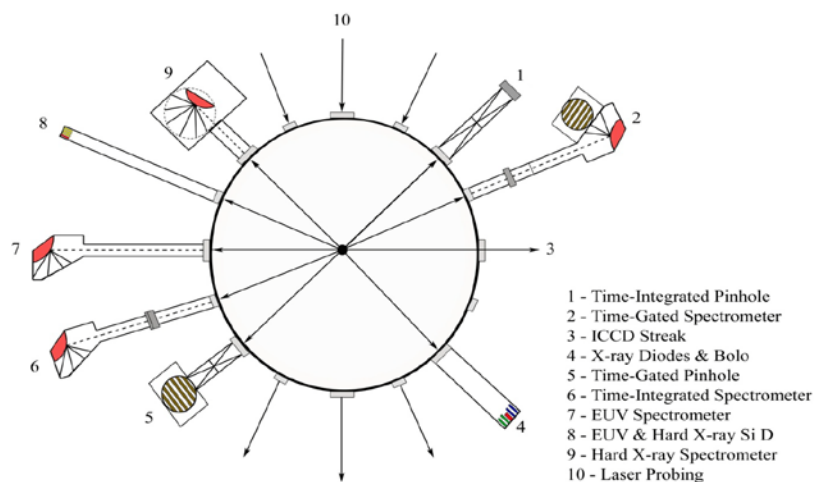


Figure 2.5. A standard arrangement for diagnostics on Zebra at NTF. Differences from campaign to campaign are typical, dependent on material and spectral range being studied.

The primarily load current diagnostics on Zebra are three equally spaced differential B-dot detectors. These detectors are able to measure load current by use of Lenz's Law. They measure induced voltage through four 3 mm diameter loops of copper during exposure to the magnetic field of the load current. The resulting voltage is proportional to dl/dt . This voltage must be stepped down by use of signal attenuators for oscilloscope readings.

The fast radiation diodes, a core component of our diagnostic capacity, are fielded in three types. The silicon diodes (SiD) used on Zebra are filtered by a direct deposition of submicron thickness Al and radiation flux is limited using pinholes. SiD detectors have a wide spectral response above 1 keV, with a maximum at approximately 3 keV. The X-ray diodes (XRD) consist of a photoelectron producing carbon cathode and a plasma-side Ni mesh that collects those electrons (Spielman, 1995). The spectral sensitivity of an unfiltered XRD detector is below 1keV. The photo conducting diode (PCD) operates differently than the previous two types of detectors. The current through the PCD is a function of the bias voltage and incident X-

ray flux (Spielman, 1995). The spectral response of an unfiltered PCD is essentially flat between 0.05-5 keV (Spielman, 1997).

The time-integrated pinhole camera (TIPH) is a relatively simple diagnostic for spatially resolving plasma parameters in six different wavelength ranges. Different filters are used to achieve this type of analysis. Pinhole images are affected by source parameters, filters employed, pinhole size, and distances between the pinhole, the source and the film. The two resolution constraints are spatial resolution and diffraction-limited resolution, with the latter more commonly referred to as the Rayleigh Criterion. Spatial resolution for this diagnostic is 220 μm .

The time-gated pinhole camera (TGPH) is a similar concept, but instead of integrating the image over the course of an entire shot, it gives snapshots over the course of some critical phase of the shot. This results in a temporal resolution of three nanoseconds in six nanosecond intervals. In order to collect images within this timeframe, a pinhole camera with a microchannel plate (MCP) imager at 230 μm spatial resolution was used. The MCP is a thin disk of lead-oxide doped glass capillaries that acts as a photomultiplier system.

The optical imaging diagnostics consist of three different systems. The first is laser shadowgraphy, which is simply the use of a laser to backlight early stage plasma parameters. A 150 ps pulse from an EKSPLA laser system is split into four pulses, partly based on polarity. Four CCD cameras then record the backlit plasma over roughly 6 ns intervals. The second optical imaging diagnostic is the ICCD. The ICCD is simply an intensified CCD camera that focuses on the pinch at some specified time during initiation or ablation and takes a focused image at a single point. It takes this image over a two nanosecond frame duration. The third diagnostic is the streak camera. A streak camera works by taking an exposure and then “streaking” it so that it can be spatially resolved in one dimension continuously over the course of the exposure. These types of images are very good at visualizing progression of a wire array as it implodes toward the z-axis.

X-ray spectroscopy is a valuable tool for directly measuring plasma parameters. If transitions can be imaged with high enough spectral resolution, theoretical models can be compared to experimental results in order to obtain the electron temperature and density of the plasma. Theoretical spectra for Cu, Fe, and Ni were produced using the Flexible Atomic Code (FAC) atomic structure code, which calculates complete atomic energy level structures, radiative, and collisional coupling data (Gu, 2008). Several spectrometers were used in these studies, primarily crystal-based and grating-based spectrometers. Both rely on diffraction in order to image a specific range of radiative transitions.

2.4 Interferometry Diagnostic Overview

The device was designed to utilize a type of interferometry known as wavefront-splitting or wave splitting interferometry. This is an in-line system in which diffractive properties of light are taken advantage of in order to disregard temporal coherence so that spatial coherence becomes the primary consideration. If the source isn't initially point-like enough at the distances established, an initial pinhole constrains the source so that it appears point-like. The first-order fringes on both sides of the airy disc pattern (Figure 1.4) are then directed into the two apertures in a secondary double-pinhole setup. The radiation entering these secondary pinholes should be of the same wavelength, spatially coherent, and in phase, thus useful for interferometry. The first-order fringes of the secondary pinholes can then be used to "bend" the radiation back to a focal point located further down the system. The theoretical application of this would be to use one first order fringe as an illumination beam for some object and to use the converging first order fringe from the other pinhole as a reference beam. The distance x , equivalent to d_3 in Figure 2.4, required so that the two theoretically identical beams converge at the middle is calculated by equations 2.1 and 2.2. In this case, λ is the wavelength of light being studied, d is the aperture diameter, y is half the distance between pinholes and θ is the angle of the diffracted light that

forms the first order constructive fringe. A loaded film holder is placed at this distance so that an exposure can be made. A basic diagram of the recording scheme can be seen in Figure 2.6.

$$\theta = \sin^{-1} 1.635 \frac{\lambda}{d} \quad (\text{eq. 2.1})$$

$$y \tan \theta = x \quad (\text{eq. 2.2})$$

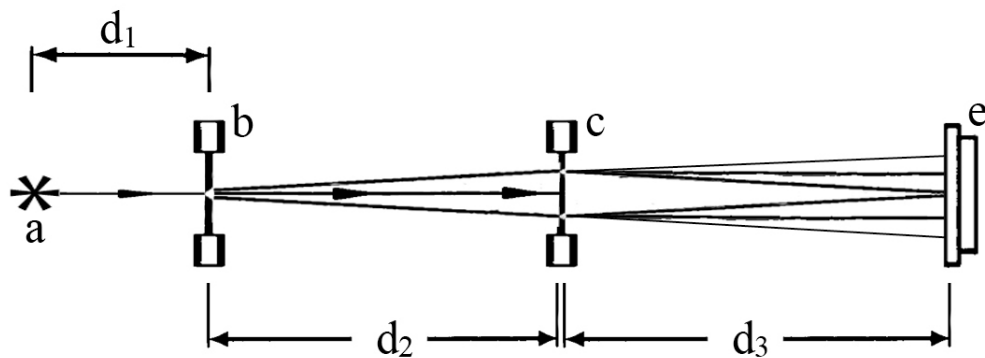


Figure 2.6. An idealized scheme for interferometric recording. a) Plasma source, from either Zebra or Sparky. b) Initial constraining pinhole. c) Double aperture unit. d₁) Distance between the plasma source and the first pinhole, which primarily affects light intensity. d₂) Distance between the first pinhole and the double aperture, which must be calculated based on the wavelength of light being studied. d₃) Distance between the double aperture and the film, which affects the resolution of the fringe patterns in the exposure. e) Film holder.

The device itself was designed to be fully adaptable to an array of applications and material types. High energy plasmas radiate in specific spectral bands relative to the materials used and their associated transitions. Because of this, the device was built so that each individual part could be adjusted to accommodate geometry requirements dependent on wavelength. In figures 2.7 and 2.8, an adaptable unit that was used as the film holder on both Sparky and Zebra is shown. It was built to be modular, affix to an optical rail, and to fit within a 4" diameter tube that could be affixed to both experimental systems. In Figure 2.8, this same unit is shown adapted as the double aperture mount.



Figure 2.7. Adjustable film mount unit. In the above figure, from left to right, it is displayed from the front, rear and side. This unit was also used to mount the double aperture, shown in Figure 5.X.



Figure 2.8. Adjustable film mount converted to mount for double aperture.

Figure 2.9 shows a similarly designed unit that was created as the mount for the primary pinhole. This design was used mainly for experiments with the laser on Sparky.



Figure 2.9. Adjustable mount for initial constraining pinhole. Pinhole shown is 250 μm .

There were a few iterations of film holder designed. The initial film holder was designed for trials on Sparky (Figure 2.10) using a screw-in, 158 nm zirconium filter, but while restructuring the experiment for Zebra, a concept with more tolerance for misalignment was designed (Figure 2.11). This version still fit the pipe diameter constraints, at the cost of being less easy to adjust for wavelength dependent geometry differences. The film used in both versions was UF-4, an emulsion film with high sensitivity in the EUV and soft X-ray wavelengths.

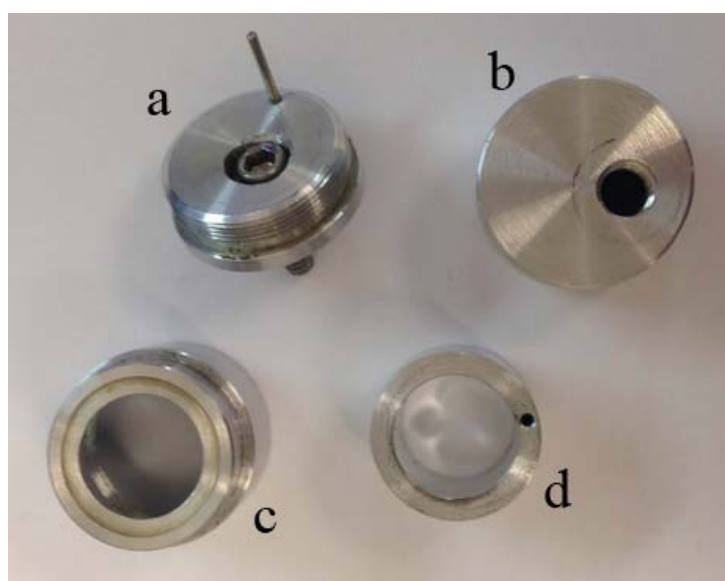


Figure 2.10. Film canister for trials on sparky. a) Film backplate. b) Filter mount. c) Filter mount holder. d) Film securing ring.

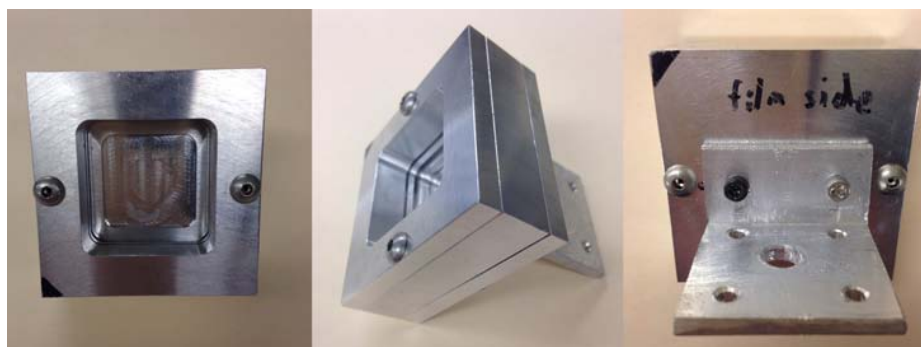


Figure 2.11. Final adjustable film mount for trials on Zebra, designed so that the front and back detach independently. The rear compartment is for the film and the front compartment is where the filter is attached. Front, side and rear views are shown from left to right.

In Figure 2.12, a shortened version of the interferometer missing the double aperture is shown. The entire device was designed in such a way that it could easily be mounted inside of a 4" tube at the film holder and a much smaller 2" tube along the rest of the length of the device. Effective total length of the system was adjustable up to 1.6 meters and with the use of 5 μm pinholes, could accommodate wavelengths down to about 4 nm. Based on calculations, lower wavelengths would require a greater distance between pinholes or smaller pinholes, which are prohibitively fragile and difficult to make, and subsequently prohibitively expensive for this type of study. A certain level of durability was required, as debris and high energy radiation could potentially destroy pinholes and other interferometer components. In Figure 2.13, a close-ups of the film holder and pinhole mount are visible.



Figure 2.12. Compacted version of interferometer for use on Zebra. The entire assembly without the double pinhole unit is shown.

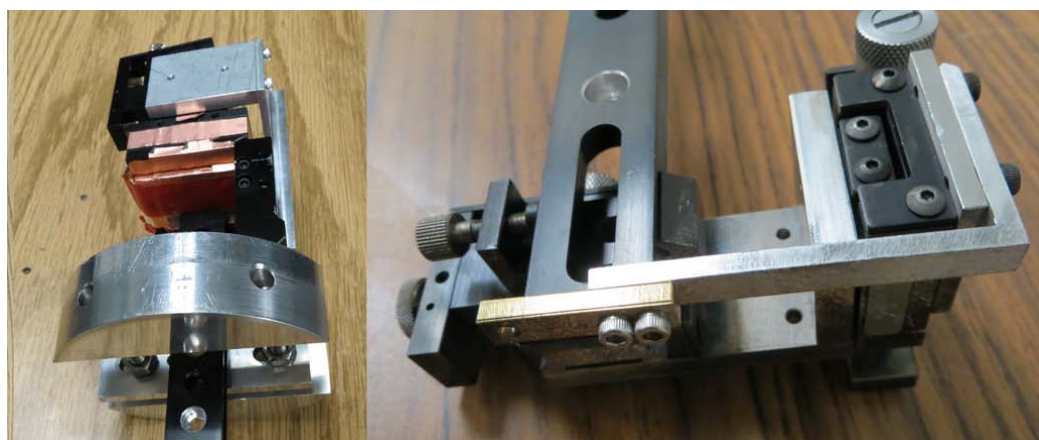


Figure 2.13. Close-up of the film holder and pipe-mount assemblies (left) and the front aperture mount (right).

Chapter 3: Single Wires at 0.9 MA

3.1 Experimental Details

All work in this chapter was performed on the Zebra generator at NTF. Array types were single wire loads (SWs) and materials used were silver as well as stainless steel, which is primarily iron and nickel. SWs have been discussed in some detail in the introduction, and as they are a relatively simple load design, further discussion of general properties will be succinct. In this section, SWs are Ag wires with a length of 20 mm and a diameter of 30 μm . They are placed directly between the anode and cathode in line with what is typically designated the z-axis, the center point on the anode and cathode structures. This orientation is demonstrated in Figure 3.1.

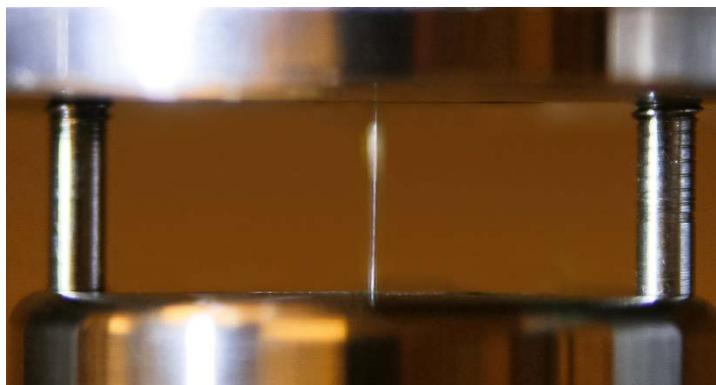


Figure 3.1. A single wire load (SW) between the anode (top) and cathode (bottom) on Zebra. The thick posts on either side of the array are removed after installation into the load chamber.

The diagnostic package used for these experiments included imaging and radiation detection systems with orientation shown in Figure 2.3. The primary diodes and their spectral sensitivities are summarized in Table 3.1. Specifically, diagnostics used were: a six-frame, dual channel, MCP-based, time-gated X-ray pinhole camera; a very high energy range photo-conducting diode (PCD) detector; an X-ray diode (XRD) detector; an extreme ultraviolet (EUV)

diode; a laser backlighting system (shadowgraphy); a time-gated EUV spectrometer; as well as a bolometer, typically either nickel or gold, depending on the research campaign at the facility.

Spectral Region	
SiD	>9 keV
PCD	>0.75 keV
XRD	>0.18 keV
EUV	>17 eV

Table 3.1. Primary diodes and their respective sensitivities.

Power measurements were obtained using a method described by Dr. Ken Williamson in his PhD Dissertation (Williamson 2011), by use of bolometer voltages and a coefficient based on the calibrated XRD detector. Zero-time for diagnostics was based around a load current threshold set at the oscilloscopes.

3.2 Radiation and Specific Shot Parameters

All loads were single wire loads. Shot 608, which was stainless steel, used a wire diameter of 25 μm with a resulting mass of 78 μg . Calculated energy output was approximately 10.0 kJ, run at a current of 0.91 MA. Shots 2459 and 2460 were both silver and 30 μm in diameter, with resulting masses of 150 μg . The energy yielded in shot 2459 was 11.0 kJ at a current of 0.83MA. The energy yielded in shot 2460 was 11.4 kJ at 0.86MA.

The significant difference in masses between the stainless steel and silver shots was due primarily to the 5 μm difference in wire diameter, but material density was also important. Stainless steel has a density of 7.93 g/cm^3 and silver has a density of 10.5 g/cm^3 . A summary of the load and implosion parameters, as well as radiation yields can be found in Table 3.2.

Shot #	Configuration	Material	Diameter	Mass	Energy	Current
608	SW	SS 304	25 μ m	78 μ g	5.0 kJ/cm	0.91MA
2459	SW	Ag	30 μ m	150 μ g	5.5 kJ/cm	0.83MA
2460	SW	Ag	30 μ m	150 μ g	5.7 kJ/cm	0.86MA

Table 3.2. Load and implosion parameters for single wire loads.

3.2.1 Silver Single Wire Loads 2459 & 2460

The Ag SW Loads described in this section were done back to back within research campaign 15 and consisted of two shots. Especially with this load type, having shots in sequence was particularly useful in determining shot-to-shot differences. The focus was to investigate characteristics of higher mid-z element silver in single wire load configuration on the Zebra generator at IMA, analyze differences in plasma parameters and radiative properties of plasmas between single wire loads and to determine where bright spot formation occurred and how predictable it might be in comparison to X-pinch loads. If bright spot formation was found to be predictable, it might not only be easier to align diagnostics for future single wire studies, but also to use single wires as a point like radiation source, similar to X-pinchs.

In figures 3.2 and 3.3, signals from shots 2459 and 2460 are displayed, in respective order, so that shot parameters over the course of the current rise can be compared. It becomes immediately clear in these figures that current rise time and overall structure over time remains similar between both shots. Radiative output is evident as early as 30ns into current start. In units of V*ns, area under each signal is comparable between both shots, which is evident in the energy calculation. The primary difference seen over the course of the shot is the variation in energy at some point in time over the first 150 ns. In shot 2459, there is an initial radiative pulse, and then two or three non-primary pulses. In shot 2460, most of the radiative output is contained within the initial primary pulse, but a secondary pulse is seen at about 70 ns. These differences in radiative properties over time indicate a high level of instability in the implosion of the SW loads.

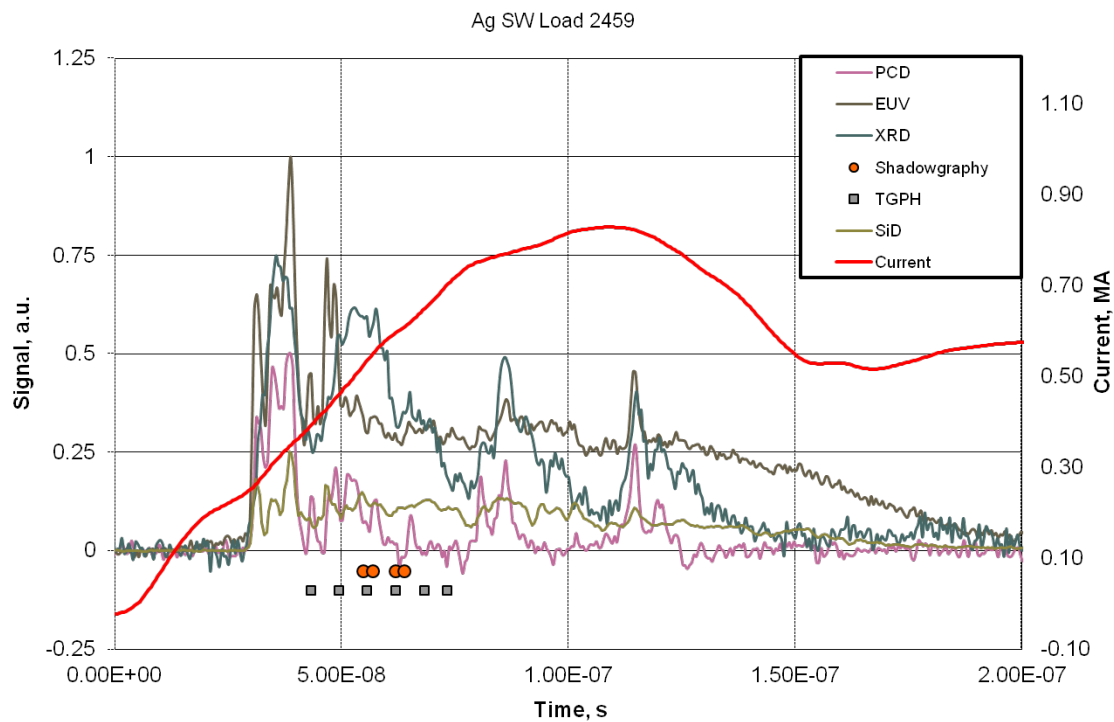


Figure 3.2. Signal Data for Zebra shot 2459.

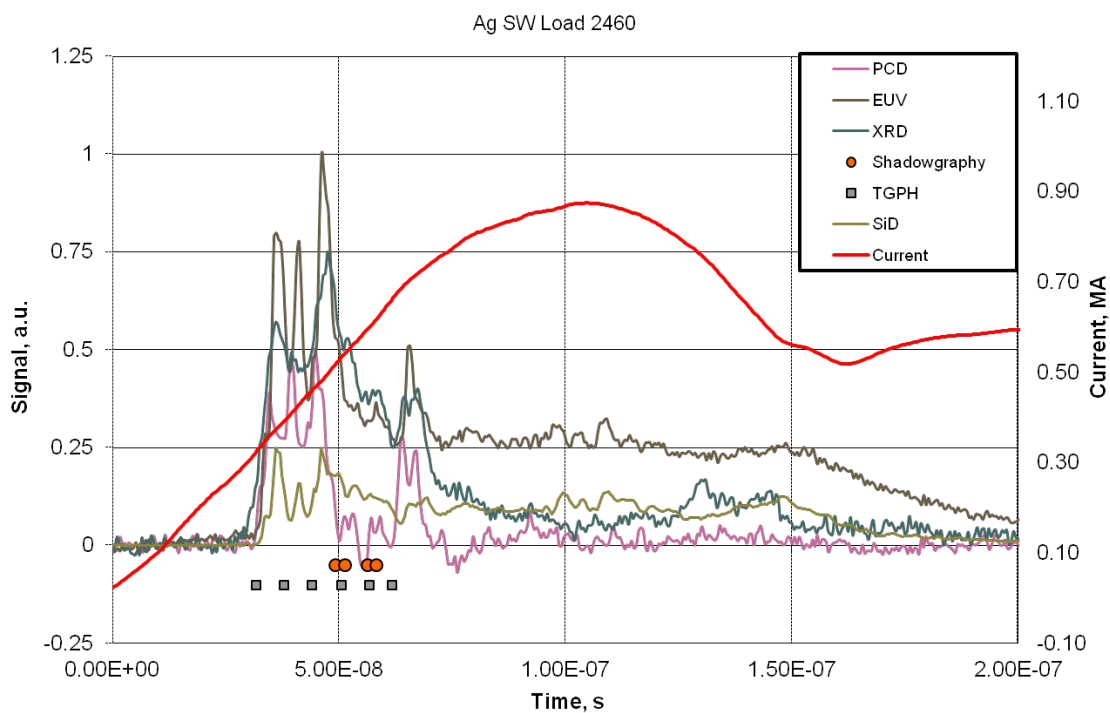


Figure 3.3. Signal data for Zebra shot 2460.

Some of these instabilities become clearer when the time gated pinhole images in figures 3.4 and 3.5 are analyzed. Over the 30 ns period in which the six snapshots are taken, bright spots appear sporadically and along the length of the wire from anode to cathode with no particular pattern. This makes sense when considering that during initiation and ablation there is a breakdown of wire core material, but in the case of a single wire load, there isn't a larger $\mathbf{j} \times \mathbf{B}$ force to form a relatively stable plasma column. Thus, in early stages, current flow and material ablation are unpredictable. To some extent, this is due to initial irregularities in wire material and load construction, but as the shot proceeds, more instabilities can be attributed to dynamics involved in wire breaking and "reconnecting" and the plasma characteristics occurring in this regime.

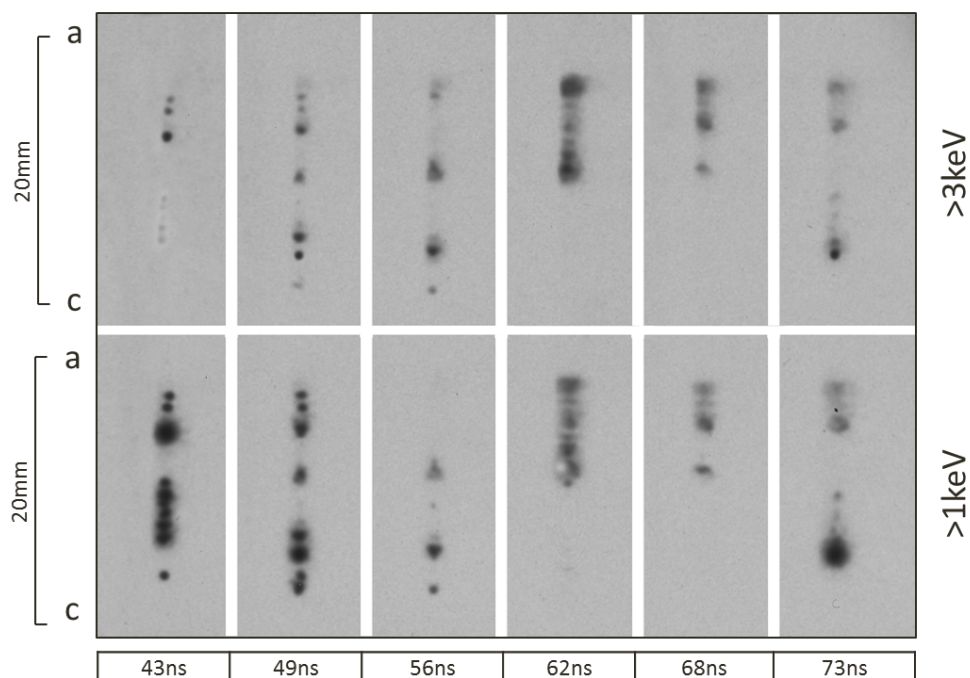


Figure 3.4. Time-gated pinhole (TGPH) images for shot 2459 filtered for >1keV and >3keV. Time is counted from current start.

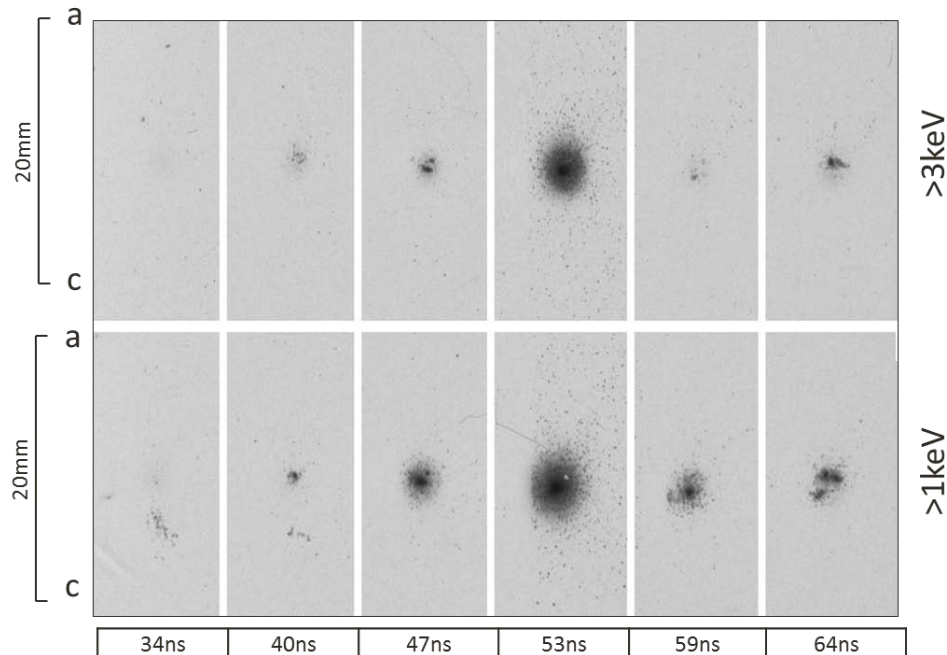
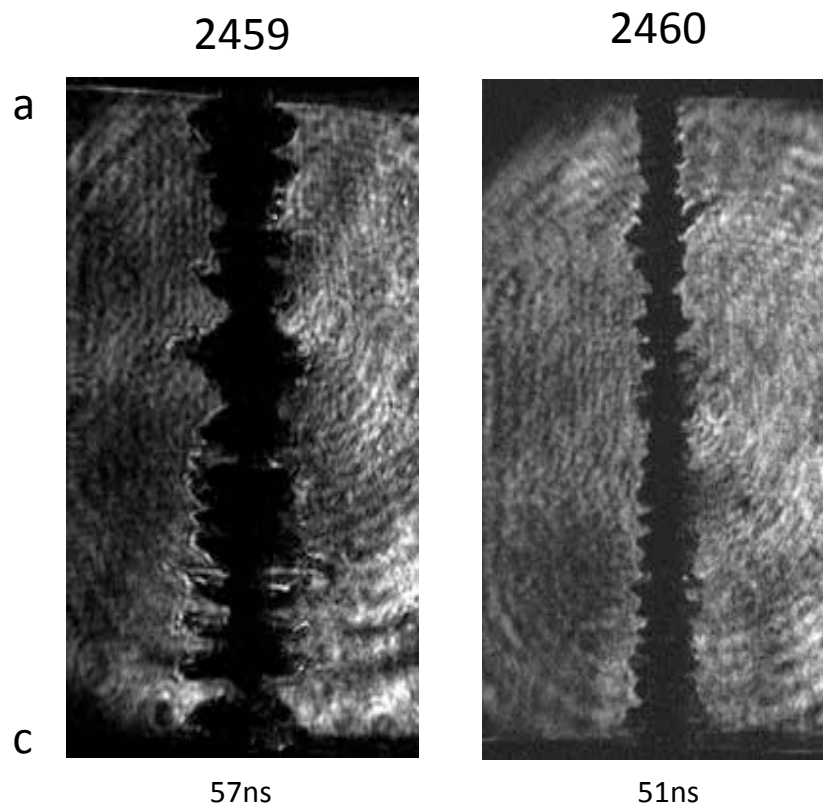


Figure 3.5. Time-gated pinhole (TGPH) images for shot 2460 filtered for $>1\text{keV}$ and $>3\text{keV}$. Time is counted from current start.

Even earlier in the shot process, significant structural instabilities can be seen. In Figure 3.6, laser shadowgraphy is used to demonstrate this phenomenon. In the laser shadowgraphy pictures, shot 2459 is captured at 57 ns and 2460 at 51 ns. For a shot that begins initiation at approximately 30 ns, this is very late for laser backlighting. Although wire material is no longer evident, the finger-like Rayleigh-Taylor magnetohydrodynamic (MHD) plasma instabilities are seen. It is hard to say whether overall plasma flow is inward or outward at this point in the process, but flow in both direction is expected as a result of these dynamics and the associated shifting magnetic field.



**Figure 3.6. Laser backlighting images from shots 2459 and 2460.
Time is counted from current start.**

Two dimensional "lineouts" are a method of taking a time-integrated or time-gated spectra and then turning it into a graph of pixel value vs. wavelength. A thin and typically uniform (vertically) section of area is selected based on location being studied between anode and cathode. This is important in establishing details about plasma parameters like density and temperature. The most important step in taking lineouts is to first identify important transitions in the material of interest from existing literature. Table 3.2 identifies some ionic transitions of importance for Ag studies, as well as the "cold" characteristic Lyman alpha and beta lines.

Diagnostic Line	Transition	Wavelength (Å)
Ag 3A	$1s^2 2s^2 2p^6 3p^1 P_1 \rightarrow 1s^2 2s^2 2p^6 ^1 S_0$	3.401
Ag 3C	$1s^2 2s^2 2p^5 3d^1 P_1 \rightarrow 1s^2 2s^2 2p^6 ^1 S_0$	3.548
Ag 3D	$1s^2 2s^2 2p^5 3d^3 D_1 \rightarrow 1s^2 2s^2 2p^6 ^1 S_0$	3.718
Ag	"Cold" $L_{\beta 1}$	3.94
Ag 3G	$1s^2 2s^2 2p^5 3s^3 P_1 \rightarrow 1s^2 2s^2 2p^6 ^1 S_0$	4.018
Ag	"Cold" $L_{\alpha 1}$	4.15
Ag	"Cold" $L_{\alpha 2}$	4.16

Table 3.3. Diagnostically important lines for silver used in this analysis.

After subtracting background and taking several spectral sensitivities into account, such as filters and film type, relative intensities based on wavelength can be determined along the z-axis. While modeling can help significantly with interpretation of these outputs, a more rudimentary examination of silver was done due to the lack of a dependable model for Ag spectra. Still, valuable information can be taken from this, such as the general temperature gradient along the z-axis. In Figures 3.7 and 3.8, this gradient is evident. While in the time gated images, it was seen that bright spot formation was sporadic, in the time-integrated image, it is clear that a larger and more diffuse plasma formation occurs nearer to the anode. By specifically analyzing the ratio of "cold" (characteristic) to "hot" (ionic) lines, it can be determined that at the anode, the colder radiation dominates and that a gradient is formed that terminates with a much higher concentration of hotter radiation at the cathode.

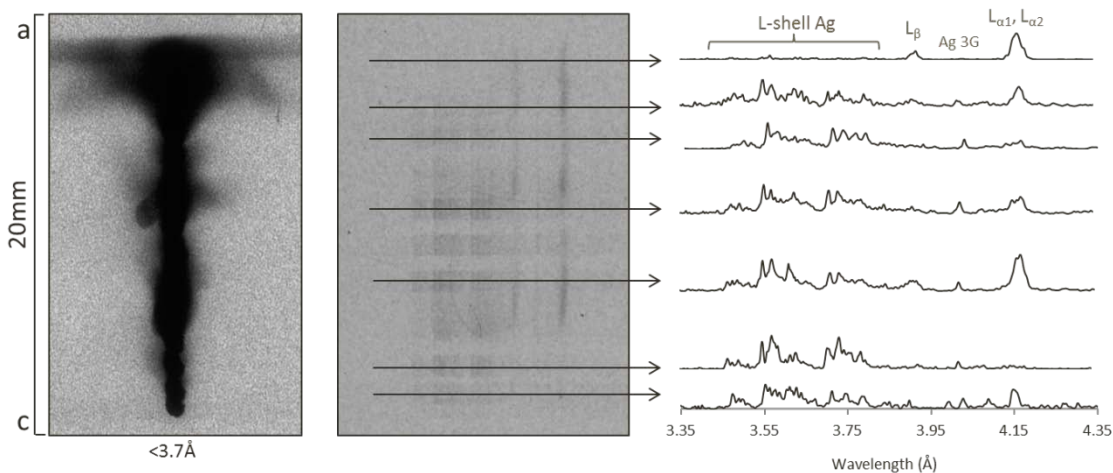


Figure 3.7. A visual and graphical analysis of gradient formed along z-axis in shot 2459.

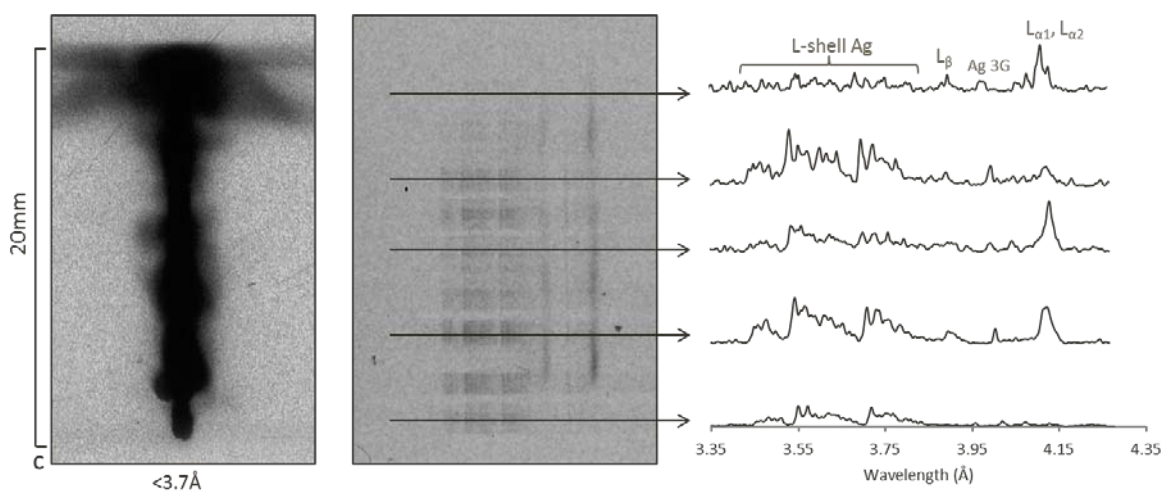


Figure 3.8. A visual and graphical analysis of gradient formed along z-axis in shot 2460.

3.2.2 Stainless Steel Single SW Load 608

Single Wire Load 608 was an earlier shot, completed in research campaign 3. The focus in this case was to investigate characteristics of mid-z elements in stainless steel 304 in single wire load configuration on the Zebra generator at IMA, analyze differences in plasma parameters and radiative properties of plasmas between single wire loads and to determine where bright spot formation occurred and how predictable it might be in comparison to X-pinch loads. In this case,

the mid-z elements involved are primarily Iron (66-74%), Chromium (18-20%), and Nickel (8-10%).

In Figure 3.9, a definite similarity with the previous single wire shots is evident. There is an early initiation, followed by an initial radiation pulse, and then approximately 20 ns later there is a second pulse, which in this case is even larger. This is again indicative of instabilities in the dynamics of how current flows through a single wire load. However, it is interesting to note that overall energy output (from Table 3.2) based on the PCD detector stays fairly consistent between single wires of a similar diameter at roughly equal top currents.

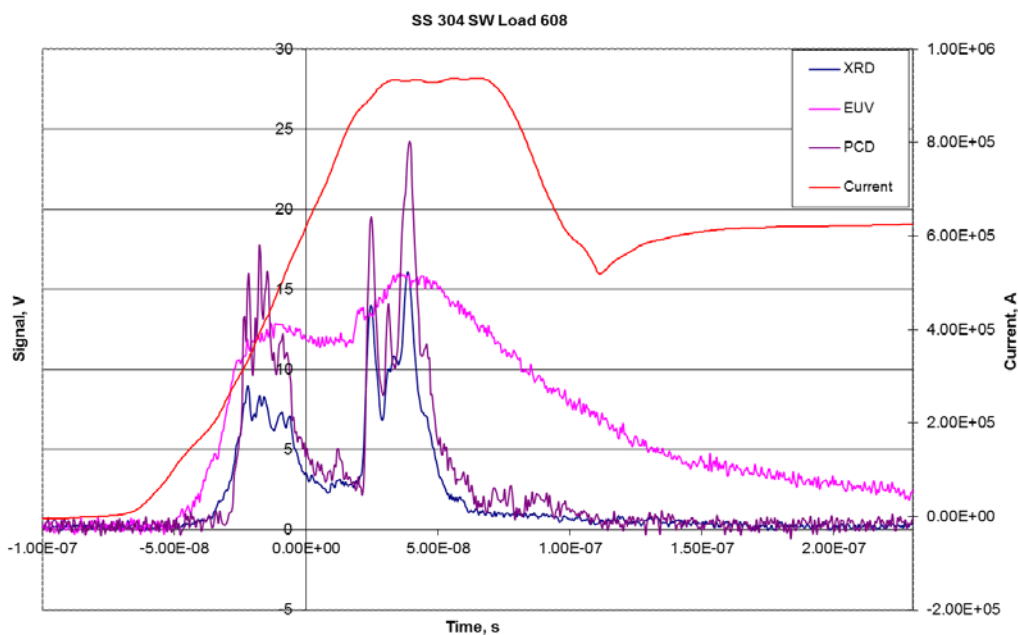


Figure 3.9. Signal data for Zebra shot 608.

Of interest is one key difference between the Ag shots 2459, 2460 and the stainless steel shot 608. By examining the left side of Figure 3.10 and comparing with figures 3.7 and 3.8, roughly comparable wavelengths, time-integrated pinhole images reveal a difference in the density and uniformity of the radiation distribution along the z-axis in that wavelength range. The Ag shots are considerably brighter and more diffuse in appearance, indicating a much greater

overall radiation in wavelengths less than approximately 3.9-4.4Å. Given that Ag L-shell transitions are directly below this cutoff likely explains this difference.

The lack of radiation in this region for stainless steel gives us an excellent opportunity to examine the distribution of bright spots in an SW. On the left, and to a lesser extent, on the right, there is a clear uniformity of “bright spots” along the length of the z-axis. This shows, in a way that is not typical for imploding shot types, that the highest energy radiation tends to be concentrated along the length of the original wire location over the duration of the shot. As we open the range of filtered radiation, it is clear that additional dynamics are at play, but there could be some use in tailoring the highest energy diagnostics to look at only the z-axis.

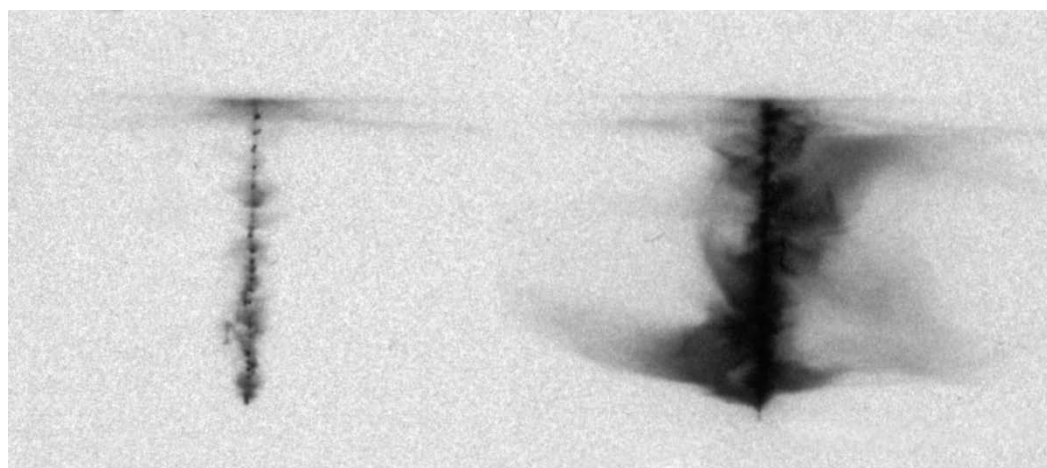


Figure 3.10. Time-integrated pinhole images for shot 608. It is filtered to show radiation below 4.4Å on the left and above 10.7Å on the right. The anode is on top and the cathode at bottom.

Similar to the methods used in the analysis of Ag, it is first important to identify diagnostically important lines for stainless steel based on previous theory and research. In Table 3.3, the primary elements that comprise stainless steel are listed with their L-shell transitions and respective wavelengths in angstroms (Ouart, 2010). Data from shot 608 was such that it could be modeled using Fe lines.

Diagnostic Line	Transition	Cr λ [\AA]	Fe λ [\AA]	Ni λ [\AA]
3A	$1s^2 2s^2 2p^6 3p^1 P_1 \rightarrow 1s^2 2s^2 2p^6 \ ^1S_0$	16.817	13.800	11.518
3B	$1s^2 2s^2 2p^5 3p^3 P_1 \rightarrow 1s^2 2s^2 2p^6 \ ^1S_0$	16.906	13.868	11.574
3C	$1s^2 2s^2 2p^5 3d^1 P_1 \rightarrow 1s^2 2s^2 2p^6 \ ^1S_0$	18.505	15.025	12.443
3D	$1s^2 2s^2 2p^5 3d^3 D_1 \rightarrow 1s^2 2s^2 2p^6 \ ^1S_0$	18.827	15.284	12.668
3F	$1s^2 2s^2 2p^5 3s^1 D_1 \rightarrow 1s^2 2s^2 2p^6 \ ^1S_0$	20.906	16.808	13.802
3G	$1s^2 2s^2 2p^5 3s^3 P_1 \rightarrow 1s^2 2s^2 2p^6 \ ^1S_0$	21.204	17.082	14.068
F1 ^a	$1s^2 2s^2 2p^4 3d \ J=5/2 \rightarrow 1s^2 2s^2 2p^5 \ J=3/2$	17.377	14.207	11.830
F1 ^b	$1s^2 2s^2 2p^4 3d \ J=3/2 \rightarrow 1s^2 2s^2 2p^5 \ J=3/2$	17.387	14.217	11.840
F2	$1s^2 2s^2 2p^4 3d \ J=5/2 \rightarrow 1s^2 2s^2 2p^5 \ J=3/2$	17.562	14.386	11.998
F3	$1s^2 2s^2 2p^4 3d \ J=5/2 \rightarrow 1s^2 2s^2 2p^5 \ J=3/2$	17.624	14.565	12.116
Na1	$1s^2 2s^2 2p^5 3s 3d \ J=1/2 \rightarrow 1s^2 2s^2 2p^6 3s \ J=1/2$	-	15.208	12.580
Na2	$1s^2 2s^2 2p^5 3s 3d \ J=1/2 \rightarrow 1s^2 2s^2 2p^6 3s \ J=1/2$	-	15.370	12.823

Table 3.4. Diagnostically important lines for stainless steel, composed primarily of iron, chromium and nickel.

To a certain extent, lines F1 and 3C were overestimated because those transitions have a degree of opacity within the plasma. Temperature and density were modeled at $T_e = 280\text{eV}$ and $N_e = 5 \times 10^{19} \text{cm}^{-3}$ for Fe. Lines 4C and 4D are typically not optically thick, and thus can be used for normalization of the model. This means that 4C and 4D can be used to magnitude adjust the modeling to match the experimental intensities so that temperatures and densities can be adjusted accordingly. The region from 13.5-14.5 \AA , primarily consists of F-like transitions and can be used in conjunction with Ne-like transitions in order to estimate temperature. The primary density diagnostics were cut off due to limitations of the spectrometer and so a common density value ($5 \times 10^{17} \text{cm}^{-3}$) for Z-pinchs of this type was used. Density changes within the surveyed spectral region will typically have the same effect as temperature changes, but at a different magnitude, so a standard value is chosen in order to better compare temperatures between similar shots or lineouts from the same shot.

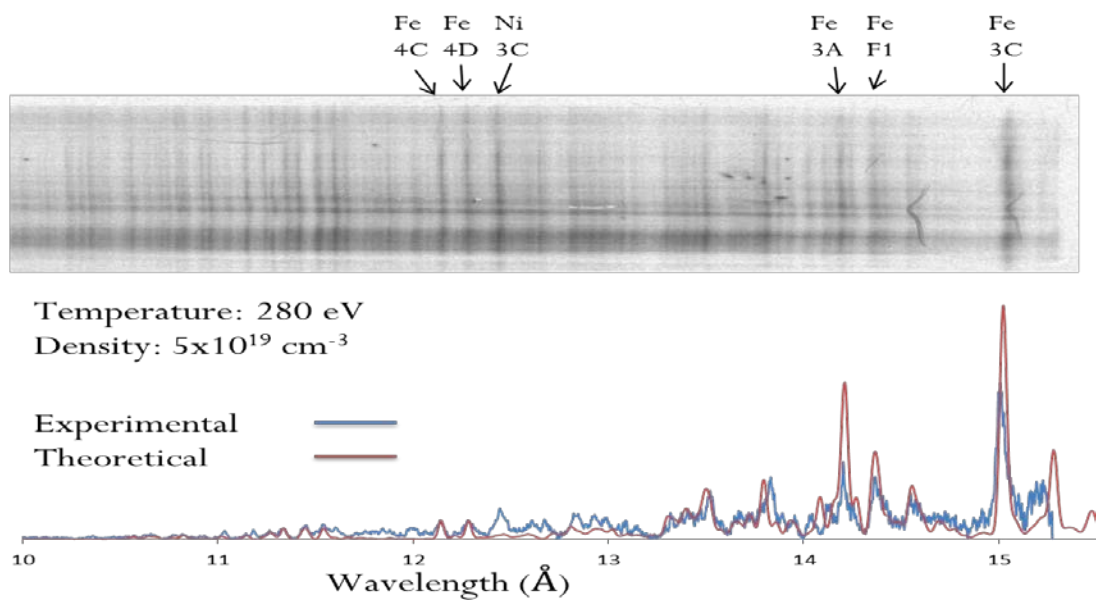


Figure 3.11. Time-integrated spectra lineout for shot 608 with a non-LTE kinetic model overlaid. Units for vertical axis are in calibrated relative intensities. Red lines are modeled and blue lines are experimental data.

Chapter 4: X-Pinches at 1-1.6 MA

4.1 Experimental Details

The focus of these studies centered on production of bright spots at the crossover point of the X-pinch at a higher current up to 1.6 MA. As with Chapter 3, all work in this chapter was performed on the Zebra generator at NTF. Array types were X-Pinches and materials used were Copper, as well as Stainless Steel. Measured differently than parallel array types, such as CWAs and PWAs, X-pinch geometry is based on the angle of the wires, which varies depending on the width and height of the wire origination position on the anode and cathode. In this case, wire angles are 62.5 degrees, usually just truncated to 62° in shot descriptions. Wire diameters were from 51-75 μm . Typical X-pinch orientation is demonstrated in Figure 4.1.

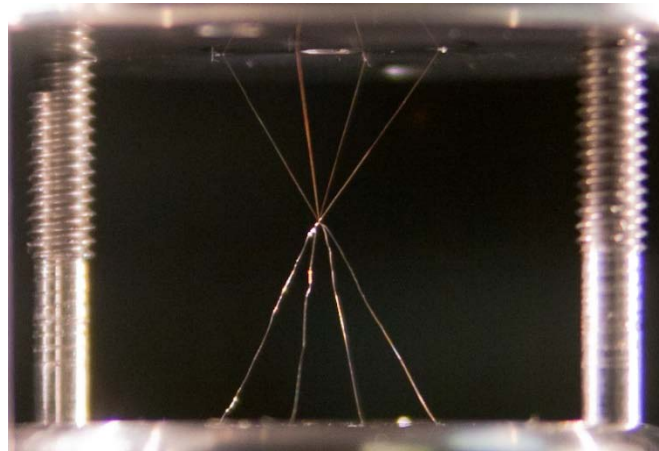


Figure 4.1. An X-pinch load on Zebra. This particular photo demonstrates that two different wire materials can be used on the top and bottom, in this case Silver and Alumel, respectively.

The diagnostic package used for these experiments included imaging and radiation detection systems with orientation similar to that in Chapter 3 and shown in Figure 2.3. The primary diagnostics, filters, and spectral sensitivities were similar as well.

4.2 Radiation and Specific Shot Parameters

Both loads studied in this chapter were X-pinches. Shot 3111, which was stainless steel, used a wire diameter of 51.4 μm , resulting in a mass of 744 μg . Bolometer energy was approximately 9.8 kJ and top current was 1.35 MA. Copper shot 3117 used a more massive 1401 μg load from a wire diameter of 75 μm . Bolo energy was 14.5 kJ and top current was 1.55 MA. A summary of the load and implosion parameters for both shots is listed in Table 4.1.

It is evident that the energy read at the bolometer for shot 3111 was significantly lower than that for 3117. Mass for shot 3111 was half that of shot 3117, and top current was also lower, which may be a factor in this discrepancy. Additionally, different materials can have significantly different radiative properties, so energy outputs between the two shots aren't necessarily comparable. Both shots were taken from a series of shots done with X-pinches at the higher LCM current on Zebra, in order to reduce differences associated with operational parameters of Zebra. However, during shot 3112, there was a capacitor bank failure that required replacement of capacitor components on Zebra. It is possible that this also introduced changes that may have affected energy readings

Shot #	Configuration	Material	Diameter	Mass	Energy	Current
3111	X-pinch	Cu	51.4 μm	744 μg	9.8 kJ/cm	1.35MA
3117	X-pinch	SS 304	75 μm	1401 μg	14.5 kJ/cm	1.55MA

Table 4.1. Load and implosion parameters for X-pinches with LCM.

4.2.1 Copper X-pinch Load 3111

Shot 3111 was completed near the end of Zebra campaign 19B. In Figure 4.2, signal data from shot 3111 is displayed. Similar to the single wire shots in chapter 3, initiation begins at about 40 ns, very early when compared to higher n, parallel array types. There is an initial

primary pulse, and then a couple of secondary pulses closer to the current max. PCD energy abates prior to 100 ns, but XRD and EUV range energy persists until approximately 200 ns.

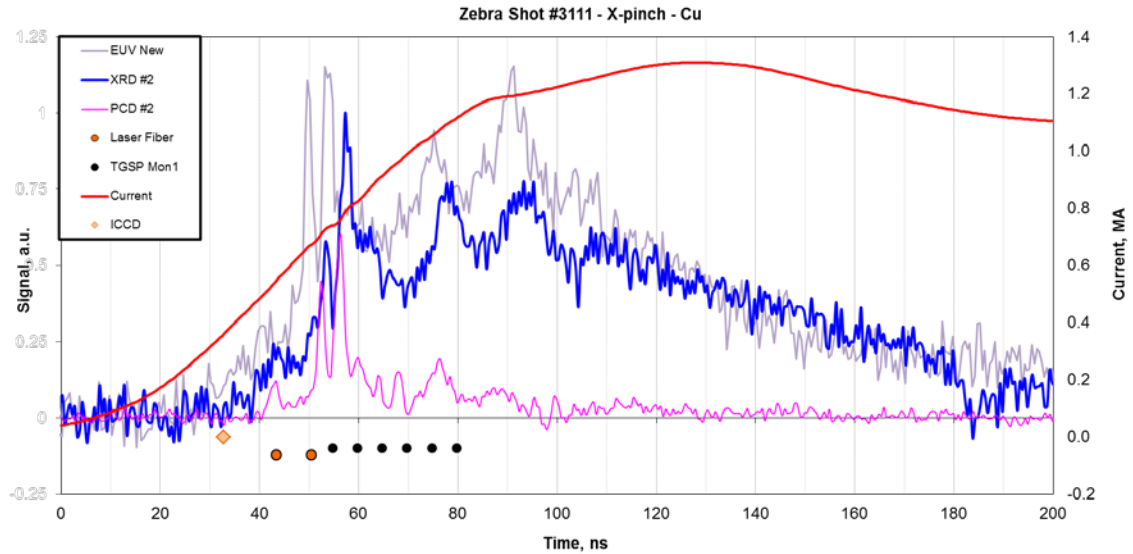


Figure 4.2. Signal data for Zebra shot 3111.

Also included in the signal data are time indicators for optical diagnostics and time-gated spectra. In Figure 4.3, ICCD and shadowgraphy images can be seen. The ICCD picture was taken at approximately 33 ns and shows the X-pinch at a very early stage. At this point, initiation has just begun and current is around 20% of maximum. In the shadowgraphy images, the pinch is backlit at about 43 ns and 50 ns. Typically with shadowgraphy, the goal is to catch the pinch at an even early stage so that the plasma doesn't block the ability to diagnose early-stage plasma parameters around the wire during initiation and ablation, but even with late shadowgraphy, the familiar finger-like Rayleigh-Taylor instabilities are evident.

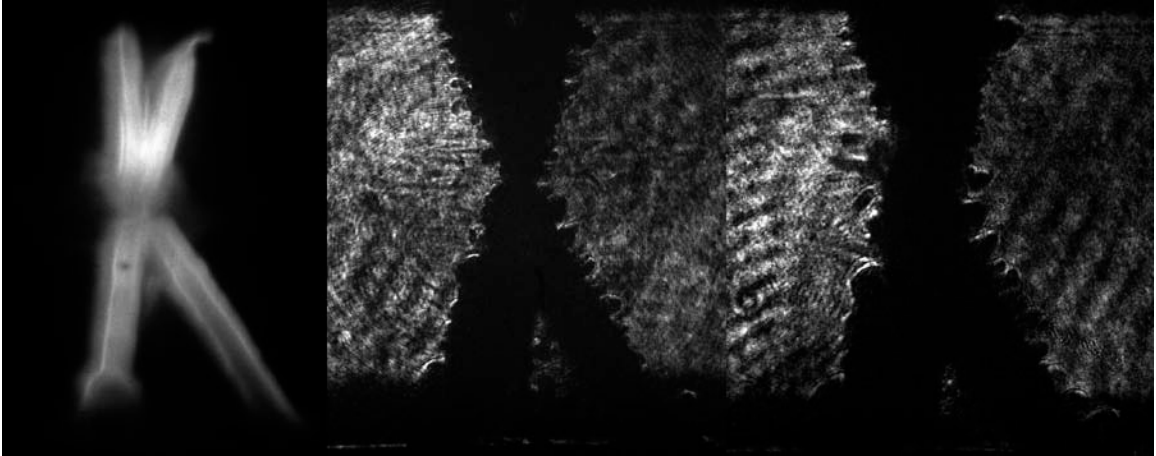


Figure 4.3. Optical diagnostics for shot 3111. Shown are ICCD (left) and shadowgraphy (middle, right) images at 43ns and 50ns, respectively.

Time gated soft X-ray spectra were also very clear in this shot (Figure 4.4). The first exposure was taken at 50ns, which in this shot was approximately the same time as the primary radiation pulse. Subsequent exposures over the approximately 6ns delays show a trend as the primary pulse temporarily abates in that the spectra in each exposure are indicative of the temperatures and densities at that moment.

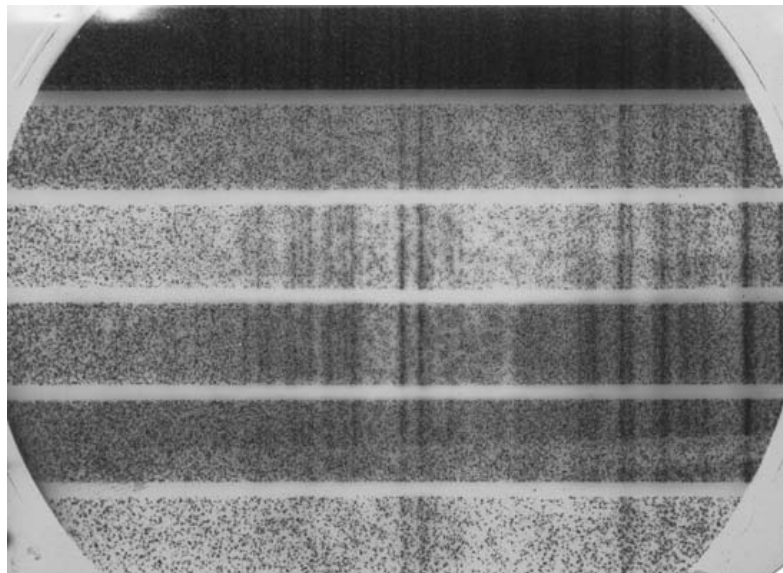


Figure 4.4. Time-gated soft X-ray spectra for shot 3111. Times (from top to bottom) are 50ns, 56ns, 63ns, 69ns, 75ns, and 80ns, counted from current start.

For Cu, important L-shell diagnostic lines are identified in Table 4.2 with their transitions and respective wavelengths in angstroms (Å). As with Ag, it's important to properly identify and label diagnostically important lines in order to apply non-LTE kinetic modeling to deduce important plasma parameters, like electron temperature and density.

Diagnostic Line	Transition	Wavelength (Å)
3A	$1s^22s2p^63p^1P_1 \rightarrow 1s^22s^22p^6\ ^1S_0$	10.580
3C	$1s^22s^22p^53d^1P_1 \rightarrow 1s^22s^22p^6\ ^1S_0$	11.390
3D	$1s^22s^22p^53d^3D_1 \rightarrow 1s^22s^22p^6\ ^1S_0$	11.608
3F	$1s^22s^22p^53s^1D_1 \rightarrow 1s^22s^22p^6\ ^1S_0$	12.591
3G	$1s^22s^22p^53s^3P_1 \rightarrow 1s^22s^22p^6\ ^1S_0$	12.849
F1 ^a	$1s^22s^22p^43d\ J=5/2 \rightarrow 1s^22s^22p^5\ J=3/2$	10.857
F1 ^b	$1s^22s^22p^43d\ J=3/2 \rightarrow 1s^22s^22p^5\ J=3/2$	10.867
F2	$1s^22s^22p^43d\ J=5/2 \rightarrow 1s^22s^22p^5\ J=3/2$	10.976
F3	$1s^22s^22p^43d\ J=5/2 \rightarrow 1s^22s^22p^5\ J=3/2$	11.123
Na1	$1s^22s^22p^53s3d\ J=1/2 \rightarrow 1s^22s^22p^63s\ J=1/2$	11.514
Na2	$1s^22s^22p^53s3d\ J=1/2 \rightarrow 1s^22s^22p^63s\ J=1/2$	11.737

Table 4.2. Diagnostically important lines for Cu.

In Figure 4.5, similar to the modeling for shot 608, 3C and F-like lines were overestimated. Again, this was due to the plasma being optically thick. Electron temperature and density were estimated at $T_e = 360$ eV and $N_e = 3 \times 10^{20}$ cm⁻³, respectively. An electron density greater than 10^{20} cm⁻³ is relatively high when compared to standard Z-pinches. The F-like lines give a good indication that a relatively high electron temperature was reached, in part due to characteristics of X-pinches.

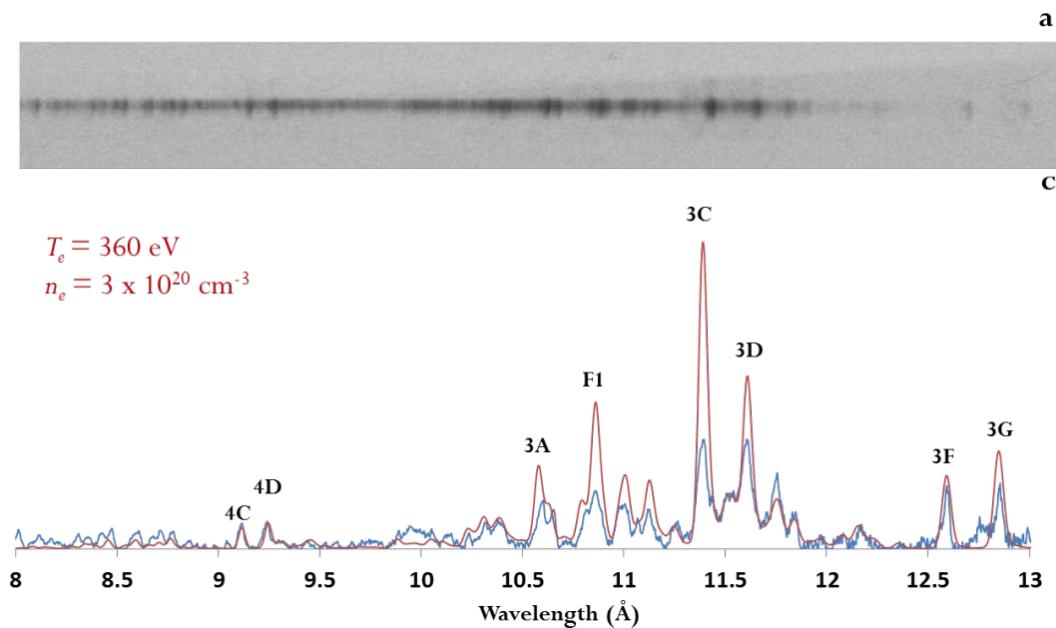
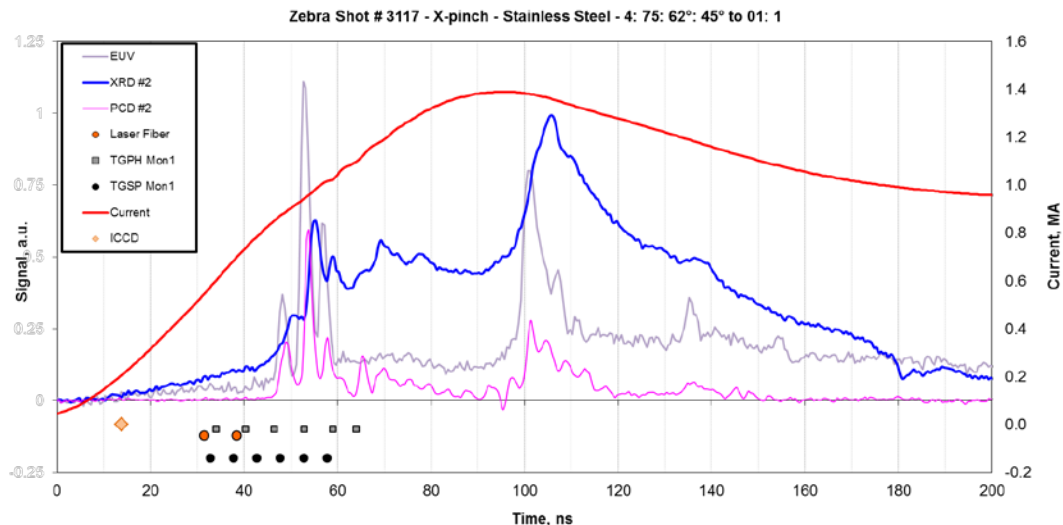


Figure 4.5. Time-integrated spectra lineout for shot 3111 with non-LTE kinetic model overlaid. Units for vertical axis are in calibrated relative intensities. Red is synthetic spectra and blue is experimental.

4.2.2 Stainless Steel X-Pinch Load 3117

An SS X-pinch, shot 3117 was recently performed on Zebra. Similar to the single wire shots in chapter 3 as well as shot 3111, initiation begins very early relative to current max. However, in the lower energy XRD and EUV ranges, signal is evident as early as current start time. Additionally, there is an initial primary pulse, as seen in other similar shot types. The difference in this case is that the primary pulse happens very quickly, followed by almost constant radiation in all measured ranges for about 30 ns. Then, at 100 ns and current peak, energy in measured ranges spikes noticeably again. By 150 ns, PCD energy is no longer evident, and then by 200 ns, radiation has abated in all but the lower energy measured spectral regions.



As with shot 3111, in the signal data are time indicators for optical diagnostics and time-gated spectra. In Figure 4.7, ICCD and shadowgraphy images can be seen. The ICCD picture was taken at approximately 14 ns and shows the X-pinch in the earliest stages of initiation. This is an excellent picture of what occurs at this stage with an X-pinch, as illumination along the wires, but particularly on the center of the load can be seen. In the shadowgraphy images, the pinch is backlit at about 32 ns and 38 ns. Although shadowgraphy images were taken at an earlier point in this shot than in 3111, it is still clear that this was after the optimal shadowgraphy timing. The reason we can say this is that the plasma formation around the ablating wires is dense enough that the area around the wires becomes completely opaque. However, in the shadowgraphy image taken at 32 ns, axial jets are evident, which is something that is well documented in previous X-pinch work (Kantsyrev, 2006). Otherwise, this shows us very little about the early-stage dynamics of the plasma parameters, other than the Rayleigh-Taylor instabilities, a common feature in every conceivable pinch type.

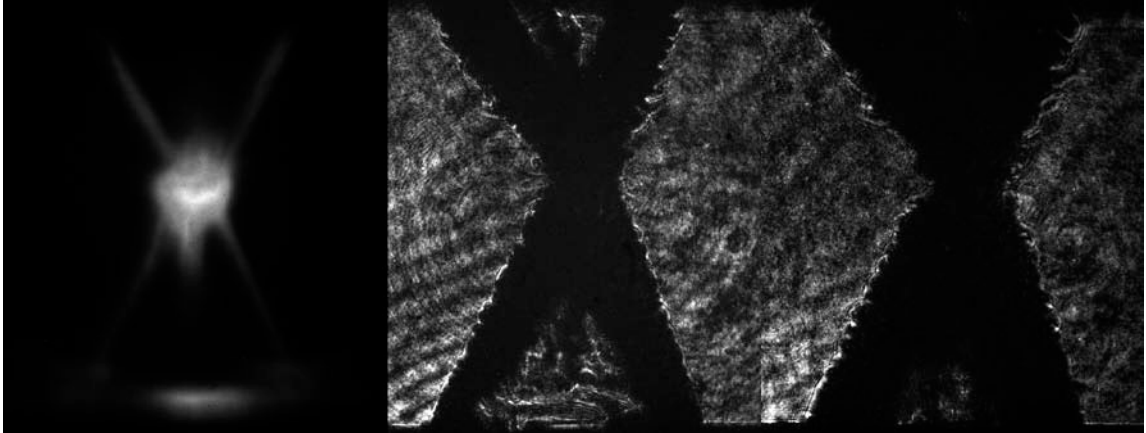


Figure 4.7. Optical diagnostics for shot 3117. Shown are ICCD (left) and shadowgraphy (middle, right) images at 32ns and 38ns, respectively.

Time-gated pinhole images in Figure 4.8 confirm the signal data, in that we see very little radiation for energy over 1keV in the first two frames. In frame three, at 47 ns and at the first sign of energy in the XRD and PCD ranges, radiation at the central crossover point on the X-pinch is evident. In frame 4, the time-gated exposure is taken right as the primary pulse occurs, and much greater energy in the $>1\text{keV}$ can be seen at the central bright spot. After the primary pulse, as radiative output temporarily drops, we see a bright spot comparable to frame 3. In this case, the analysis for time-gated pinhole images is useful for determining that the majority of the high energy radiation is originating at the crossover point in the center of the X-pinch.

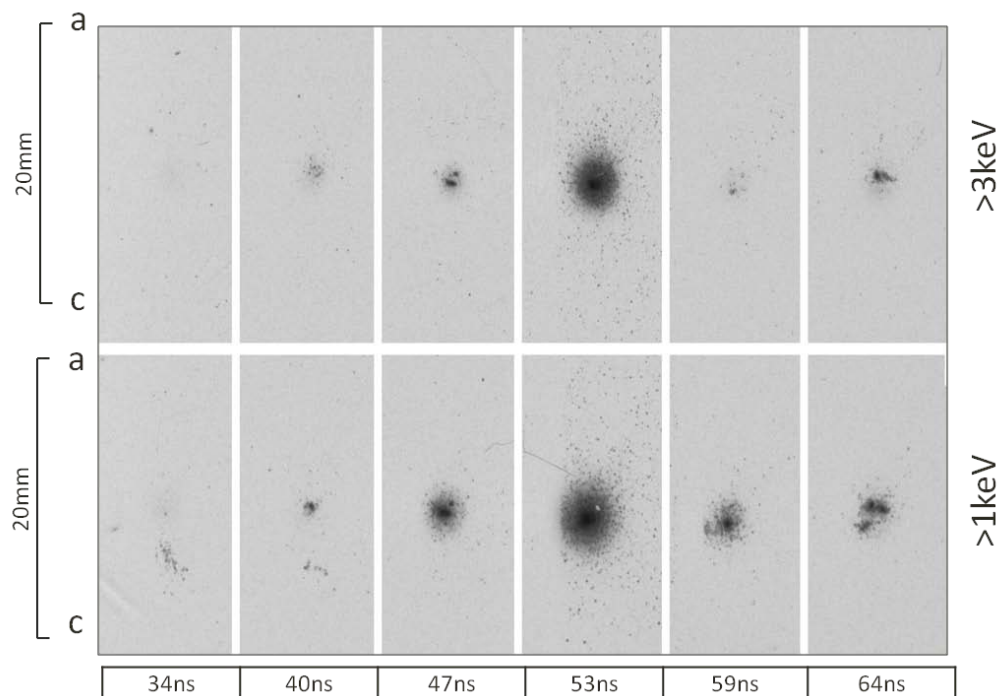


Figure 4.8. Time-gated pinhole images for shot 3117 filtered for >1keV and >3keV. Time is counted from current start.

Time-integrated pinhole films (Figure 4.9) show a similar story. With such a high mass load, the majority of the high energy radiation is concentrated at the central point. At the highest energy cutoff, in which only radiation below 10\AA passes through the filter, radiation from the wires is only barely visible. Typically, radiation from the wires closest to the anode is obvious, sometimes as bright as the central point. For shot 3117, this is not the case, with only a very limited amount of high-energy radiation being emitted along that portion of the wires.

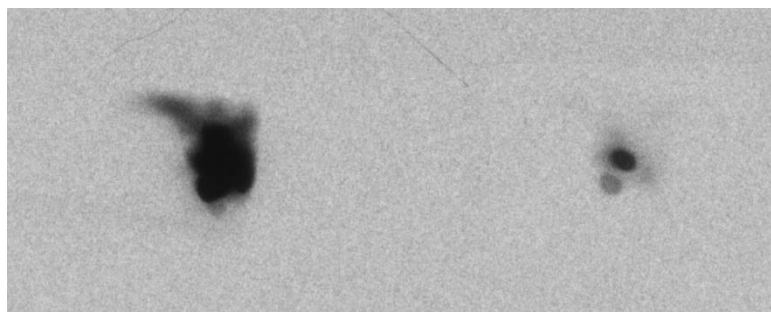


Figure 4.9. Time-integrated pinhole images for shot 3117. Image on the left is filtered at >1keV and image on right is filtered at >3keV.

Unfortunately, the spectra recorded in the time-integrated spatially-resolved images wasn't optimal for modeling temperature and density for Fe or Cr. In Figure 4.10, in the darker band on the right, there is evidence of other transitions, but most of these lie well below the wavelengths for known L-shell Fe. There is clear evidence of Ni transitions, which means that there is strong radiation in general. This statement can be made because Ni only composes about 10% of the material in SS 304, so evidence of Ni correlates somewhat to higher overall radiation output.

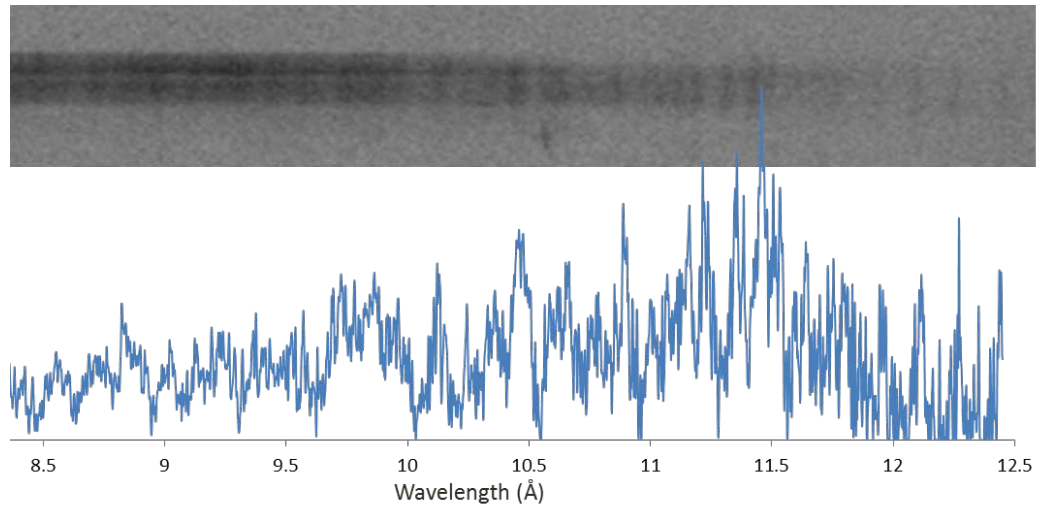


Figure 4.10. Time-integrated spectra lineout for shot 3117. Temperature and density modeling was inconclusive.

Chapter 5: X-ray Wavefront Splitting Interferometry Investigations

5.1 Nature of the Source

The primary goal in the interferometry investigations was to see if it was possible to produce a light source by z-pinch or laser produced plasma that could be bright enough and in a high enough energy wavelength in order to do EUV or X-Ray range interferometry. The experimental equipment utilized were the Z-pinch pulsed power generator at the Nevada Terawatt Facility, Zebra, and the continuum laser in the Sparky Facility operated by Dr. Victor Kantsyrev in the Leifson building at UNR.

The film used was a UF-4 emulsion film, which was investigated previously by Bessarab (2000) for its spectral sensitivity in the 0.27-3 keV range. It has also been used previously in our research group for studies with a specialized Thomson parabola (Nishio, 2012). It was suitable for these studies because the radiation being investigated was either in the EUV range at 17 nm, or the soft X-ray range at about 4-5 nm. Based on the studies by Bessarab, photon density on the film is approximately 10^9 photons/cm³ at 0.25keV and flattens out at about 10^8 photons/cm³ between 1.5-3 keV.

5.2 Experiments on Sparky Facility

Experiments on Sparky were done using the laser system described in Chapter 2. Initially, the plasma jet was assumed to be small enough to act like a point source at the distances used to the double aperture. As a trial for future studies on Zebra, a Cu target was used with a focus on M-shell transitions, which predominantly occur at 17 nm (Safronova, 2006). Assuming radiation at this wavelength and utilizing a double aperture with 30 μ m pinholes, the required distance between the double aperture and the film in order to overlap both first order fringes was found to be 1.08 m. The method for these calculations is found in Chapter 1. A 0.158 μ m

zirconium filter was utilized to limit radiation in such a way that radiation would be constrained to less than 20 nm for a cleaner interferogram with a limit on the higher wavelengths overlapping at the central region of interest.

In subsequent shots, an initial pinhole was employed and distances were recalculated based on the angle for the first order fringes from the initial pinhole at 17nm. In Table 5.1, all 19 trials are summarized. No image was obtained on the first trial. On the second trial, an image was obtained and all shots afterward yielded exposures. Shot 10 was set aside without the use of the laser plasma to ensure that exposures were not due to light penetrating the tungsten filter.

Shot #	Date	Configuration	Exposures
1	9/17/12	250 μ m	~250
2	9/19/12	250 μ m	~1000
3	9/20/12	2 x 30 μ m	~3000
4	9/21/12	250 μ m	~1680
5	9/21/12	2 x 30 μ m	~5000
6	9/25/12	2 x 30 μ m	~10000
7	9/26/12	250 μ m	~1500
8	9/28/12	1 x 30 μ m (\uparrow)	~10000
9	9/28/12	1 x 30 μ m (\downarrow)	~10000
10	10/1/12	250 μ m	0
11	10/2/12	250 μ m	~1200
12	10/3/12	1 x 30 μ m (\downarrow)	~10000
13	10/3/12	1 x 30 μ m (\uparrow)	~10000
14	10/8/12	2 x 30 μ m	~10000
15	10/10/12	2 x 30 μ m	~10000
16	10/11/12	2 x 30 μ m	~7500
17	10/12/12	2 x 30 μ m	~3300
18	10/16/12	2 x 30 μ m	~1100
19	10/17/12	2 x 30 μ m	~1100

Table 5.1. Summary table of all shots performed on Sparky. Arrows on shots 8, 9, 12, and 13 indicate that one hole was closed.

Trial 19 was the final trial done on the Sparky facility and yielded the best film exposure with the least amount of shots. In this case, using two 30 μm pinholes, an image was obtained in 1,100 shots that was darker than a prior image that had been created using about 10,000 shots. The assumption at this point was that this exposure represented a high level of alignment and could be an interferogram, constrained by the 1 mm aperture that held the zirconium filter—hence the small circular shape of the exposure. Experiments on Sparky were stopped at this point and trial 19 was saved for possible illumination and reconstruction. Results are discussed below in section 5.5.

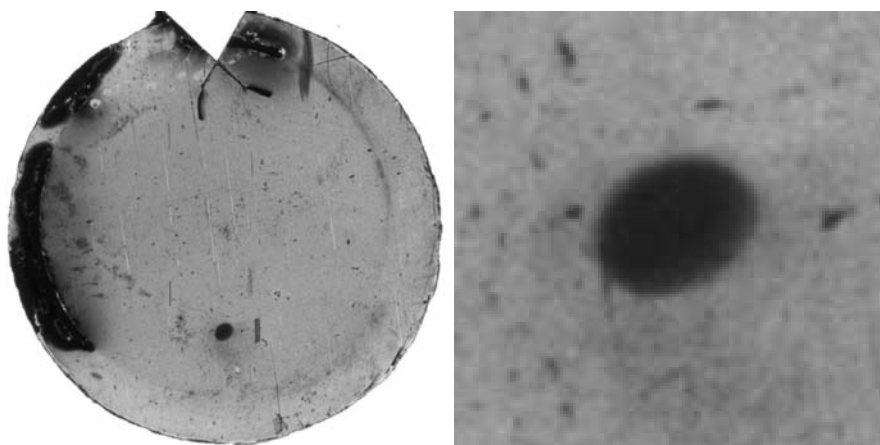


Figure 5.1. Trial 19 on Sparky with two 30 μm apertures and ~1100 exposures. On the right is a magnification of the exposure.

5.3 Experiments on the Zebra Generator

On Zebra, a considerable redesign had to be made. The film canister in Figure 2.10 was replaced with a film holder that could accommodate different filter types, which is pictured in Figure 2.11. The modular nature of the system made it possible to easily recombine the Sparky setup so that each component could be reutilized in some way on Zebra, though some switched functions. Rather than the 0.158 μm zirconium filter used in the Sparky trials, three different

materials were used. An aluminized mylar filter, with an Al thickness of 0.2 μm total and mylar thickness of 1 μm , was layered on top of a polypropylene filter with a thickness of 2 μm . The relative intensities of radiation expected from this combination matched with a sample mid-z L-shell spectra are shown in Figure 5.2. Maximum transmission of 10% within the range of interest occurs between 4.3 nm and 5 nm.

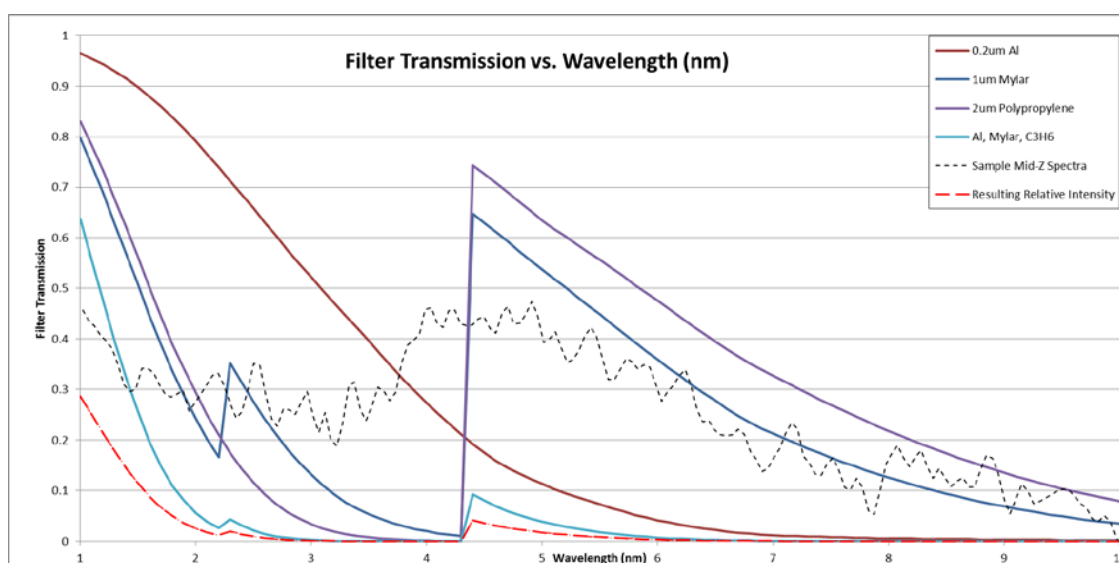
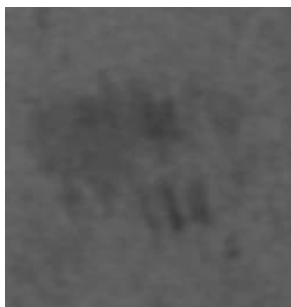


Figure 5.2. Filter transmissions for Al, mylar, and polypropylene and all three combined. Sample mid-z L-shell spectra is included with an expected intensity after filtration.

There were 5 trials done for interferometry on Zebra. In the final trial, shot 3119, reflections that had caused overexposure in previous shots were fixed and interferometric results were obtained. In Figure 5.3, the convergence point for both first-order fringes is magnified, showing an expected interference pattern.

Shot #	Configuration	Material	Diameter	Mass	Energy	Current
2997	X-pinch	Mo	50.8 μm	732 μg	20.0kJ/cm	1.12MA
3113	X-pinch	SS 304	50 μm	623 μg	11.1kJ/cm	1.47MA
3114	X-pinch	SS 304	38.1 μm	361 μg	13.1kJ/cm	1.17MA
3119	X-pinch	Cu	133 μm	4979 μg	11.9kJ/cm	1.58MA

Table 5.2. Load and implosion parameters for X-pinches with LCM.



**Figure 5.3. Magnification of area of interest in shot 3119.
Exposure width is about 1.4 mm.**

5.5 Image Reproduction

An attempt at image reproduction was performed after interference patterns were acquired. The basic scheme consisted of a 633 nm single-mode laser and a geometric magnification setup using optics with a magnification lens. The resulting image was recorded digitally and then examined for features consistent with a reproduction image. The reproduction diagram is shown in Figure 5.4. d_1 was 15 cm and d_2 wasn't utilized in the final scheme. d_3 was approximately 3.2m. The magnification of the image was found to be approximately 35 times the original.

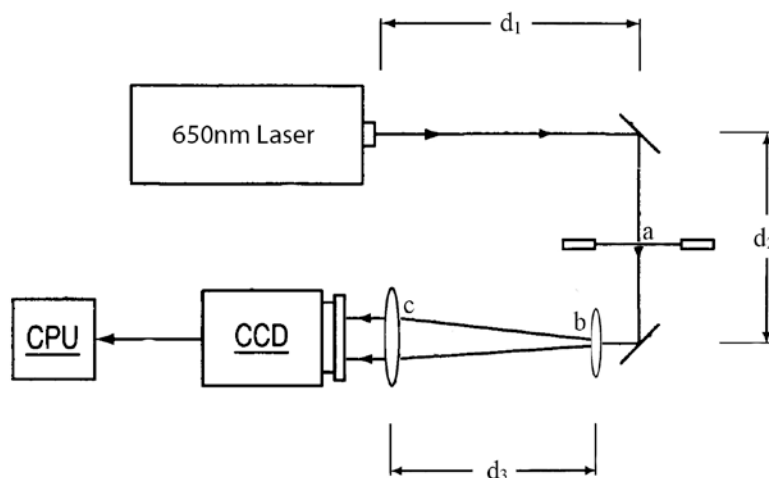


Figure 5.4. Reproduction diagram. a) Film with stored image. b) Magnification Lens for expanding image. c) Refocusing Lens. For focusing magnified image on CCD. d_1 - d_3) Distances associated with reproduction scheme. 1 and 2 are arbitrary, whereas 3 is based on degree of magnification.

In Figure 5.5, the image produced from the re-illuminated exposures created at the Sparky facility are shown. An image was obtained, but no reproduction characteristics are evident. It is possible that the speckle pattern on the right is interferometric in nature, but without an illuminated object beam to analyze, little diagnosis can be made.

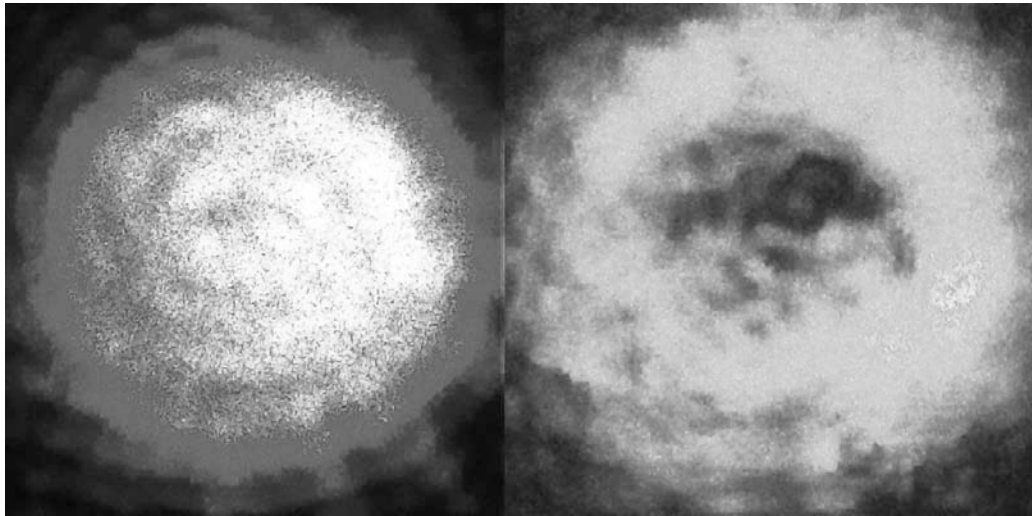


Figure 5.5. Reproduction of image from experiment #19 on Sparky facility. Background produced without film (left) and reproduction of interferometry image (right).

In Figure 5.6, a better case can be made. Interference effects are similar to those found in Figure 5.5, however, interference fringes can be seen in the center-right portion. By use of these fringes, resolution can be calculated and compared with expected values. Geometric magnification of the image was approximately 35 times the original. The fringe widths on the illuminated image were 0.8 cm, resulting in an original image fringe width of 0.23 mm. This falls outside of the calculated range of 0.31-0.93 mm, but only barely. It's easy to conclude that interference effects are within the order of magnitude of which they were expected, but it is difficult to decipher what experimental factor resulted in the fringe width calculated being outside of range. A number of effects could be the cause, including differences in the geometry of the diagnostic vs. the idealized concept as well as measurement errors.

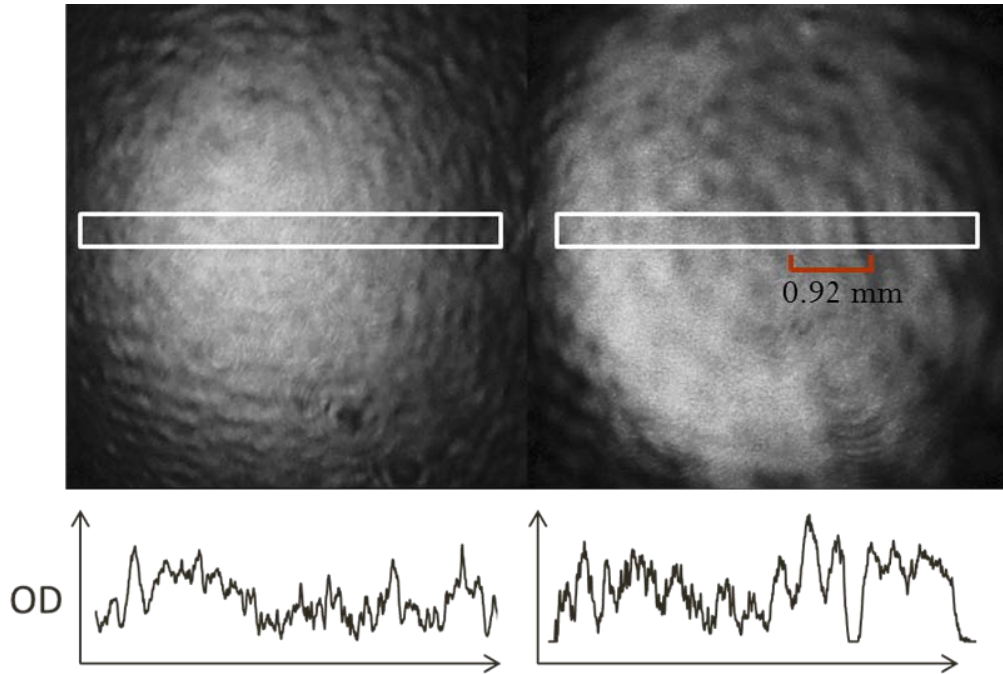


Figure 5.6. Reproduction of interferometry image acquired during Zebra shot 3119. Background produced without film (left) and reproduction of interferometry image (right). An interference pattern is visible on the right half of the right image. Measured distance between fringes was 0.23 mm. For the lineouts at bottom left and bottom right, vertical axis is optical density (OD) and horizontal axis is distance in mm.

Chapter 6: Conclusion

6.1 X-pinches and Single Wire Loads

Both X-pinches and SW load types have very early initiation (well before max current at approx. 100ns), from 25ns to 50ns after current start. Their bright spot formation seems comparable. However, X-pinch bright spot formation is more centralized along the wire crossover point in an area within a 2 mm radius from that point, dependent on current peak.

In comparing research done in this thesis to experiments done by previous groups at NTF (Safronova, 2006; Kantsyrev, 2006) it can be seen that at 0.9 MA, X-pinches and SWs have similar total radiation yields, and both load types produce a multiple burst X-ray radiation pulse. With currents in the range of 1.3-1.6 MA, significantly higher radiation yields per unit length are found. Compared to lower current shots, energy output measured at the bolometer is multiplied by a factor of about approximately double. For example, in a previous study of X-pinches at standard Zebra current, Fe X-pinches yielded energies in the range of 3.5-4 kJ/cm (Kantsyrev, 2003). In the research done for this thesis, energies for SS 304 (primarily Fe) were measured between 11-13 kJ/cm.

Signal data determined that EUV and X-ray energy are similarly distributed when comparing both X-pinches and SWs at 0.9 MA, with the vast majority of EUV radiation being produced after the main pulse. This was true for X-pinches on Zebra at currents up to 1.6 MA as well.

It is evident in all SW loads that a plasma temperature gradient along the z-axis by observing ratios in the optical density of ionic radiation transitions (Ag 3A, 3C, 3D, etc.) and characteristic radiation transitions (L_{α} , L_{β} , etc.) exists, a trend toward "colder" plasma at the anode region and "hotter" plasma at the cathode region is observed. X-pinches may have a temperature/energy gradient along the z-axis as well, but most of the radiative output comes from the central crossover point in the load.

6.2 Interferometry

It was concluded that Zebra does in fact produce enough radiative energy in the "water window" wavelengths, approximately 2-5 nm, in order for further investigation of interferometry for biological specimens to be a viable path for research. Atomic transitions for many mid-Z elements, including copper, should yield radiation within this range at intensities appropriate for single shot interferometric imaging. Particularly for the interferometry investigations, the brighter and smaller the point of radiation, the better the potential for high resolution interferometry.

In X-pinch shot 3119 performed on the university scale Z-pinch generator, Zebra, an interferometric pattern was observed. The difference in calculated fringe width was likely due to a lack of monochromatization, in that weaker radiation from the 2-2.5 nm wavelengths band may have impacted the interference patterns in such a way that the fringe widths were different than the expected values.

Recommendations for future research would be to use smaller pinholes (if available) for higher resolution imaging, or to attempt the interferometry with slits rather than apertures, for more vertical alignment tolerance. A higher level of monochromatization, made possible with a multilayer mirrors, crystals or diffraction grating could prevent other wavelengths from producing aberrations in expected interferograms. Another suggestion would be that alignment methods could be improved, allowing a greater rate of shots per successful interferogram. The design for this interferometer was based on an idealized concept of the point source properties of radiation produced by X-pinches and single wires, and so future revisions of the device should be more robust in order to consider wider plasma parameters and less ideal point-like source properties.

References

- Ampleford, D. J., Lebedev, S. V., Bland, S. N., Bott, S. C., Chittenden, J. P., Jennings, C. A., Kantsyrev, V. L., Safronova, A. S., Ivanov, V. V., Fedin, D. A., Laca, P. J., Yilmaz, M. F., Nalajala, V., Shrestha, I., Williamson, K. M., Osborne, G. C., Haboub, A., Ciardi, A. "Dynamics of conical wire array Z-pinch implosions." *Phys. Plasmas* 14 (2007): 102704.
- Bailey, J. E., Smelser, R., Nielson, D. S., Nash, T. J., MacFarlane, J. J., Lake, P. W., Jobe, D., Heeter, R. F., Foord, M. E., Cuneo, M. E., Cohen, D., Chandler, G. A., Torres, J. "Radiation science using Z-pinch x rays." *Phys. Plasmas* 9, (2002): 2186.
- Bauer, B. S.; Kantsyrev, V. L.; Winterberg, F.; Shlyaptseva, A. S.; Mancini, R. C.; Li, H.; Oxner, A. "Proceedings of the Fourth International Conference on Dense Z-pinchs." *AIP Conf. Proc.* 153 (1997): 409.
- Bessarab, A. V., Pospelova, S. A., Tokarev, V. A., Chukalovskii, A. V. "Spectral Sensitivity of the $\gamma\phi$ -4 Photographic Film in the 0.27-3 keV Range." *Instruments and Experimental Techniques* 43(4) (2000): 573-575.
- Chuvatin, A. S.; Kantsyrev, V. L.; Rudakov, L. I.; Cuneo, M. E.; Astanovitskiy, A. L.; Presura, R.; Safronova, A. S.; Cline, W.; Williamson, K. M.; Shrestha, I.; Osborne, G. C.; LeGalloudec, B.; Nalajala, V.; Pointon, T. D.; Mikkelsen, K. A. "Operation of a load current multiplier on a nanosecond mega-ampere pulse forming line generator." *Phys. Rev. ST Accel. Beams* 13 (2010): 010401.
- Esaulov, A. A.; Kantsyrev, V. L.; Safronova, A. S.; Velikovich, A. L.; Cuneo, M. E.; Jones, B.; Struve, K. W.; Mehlhorn, T. A. "Magnetostatic and magnetohydrodynamic modeling of planar wire arrays." *Phys. of Plasmas* 15 (2008): 052703.
- Fedin, D. A., V. L. Kantsyrev, A. S. Shlyaptseva, M. D. Mitchell, B. M. Song, S. A. Pikuz, T. A. Shelkovenko, K. M. Chandler, D. A. Hammer, Maxson, L. M. "Investigation of the radiation properties of L- and M-shell X-pinch plasma x-ray sources using a transmission grating spectrometer." *Review of Scientific Instruments* 75(10) (2004): 3711-3713.
- Fedin, D. A. "Experimental characterization of high current X-pinch plasma source and study of the influence of an energetic electron beam on the source parameters." Diss. University of Nevada, Reno, 2004. Print.
- Gu, M. F. "The flexible atomic code." *Can. J. Phys.* 86 (2008): 675-689.
- Hammer, D. A., Sinars, D. B. "Single-wire explosion experiments relevant to the initial stages of wire array z pinches." *Laser and Particle Beams* 19 (2001): 377-391.
- Kantsyrev, V. L., Fedin, D. A., Shlyaptseva, A. S., Hansen, S. B., Ouart, N., Chamberlain, D. "High-Z 0.9–1.0 MA X-pinch as a possible backlighter in 50–100 keV and sub-keV-10 keV spectral regions and a powerful soft x-ray source for surface modification research." *Review of Scientific Instruments* 74(3) (2003): 1935-1938.

Kantsyrev, V. L., Fedin, D. A., Shlyaptseva, A. S., Mitchell, M. D., Song, B., Pikuz, S. A., Shelkovenko, T. A., Chandler, K. M., Hammer, D. A., Maxson, L. M. "Studies of energetic electrons with space and time resolution in Mo and W X-pinches from measurements of x rays >9 keV." *Review of Scientific Instruments* 75(10) (2004): 3708-3710.

Kantsyrev, V., Safronova, A., Ivanov, V., Fedin, D., Mancini, R., Astanovitsky, A., Legalloudec, B., Batie, S., Brown, D., Nalajala, V., Shrestha, I., Pokala, S., Ouart, N., Yilmaz, F., Clinton, A., Johnson, M., Cowan, T., Jones, B., Coverdale, C. A., Deeney, C., Lepell, P. D., Jobe, D., Nielson, D. "Radiative properties of asymmetric and symmetric X-pinches with two and four wires recently produced on the UNR IMA Zebra generator." *Journal of Quantitative Spectroscopy & Radiative Transfer* 99 (2006): 349-362.

Kantsyrev, V. L.; Rudakov, L. I.; Safronova, A. S.; Fedin, D. A.; Ivanov, V. V.; Velikovich, A.L.; Esaulov, A. A.; Chuvatin, A. S.; Williamson, K. M.; Ouart, N. D.; Nalajala, V.; Osborne, G. C.; Shrestha, I.; Yilmaz, M. F.; Pokala, S.; Laca, P. J.; Cowan, T. E. "Planar Wire Array as Powerful Radiation Source." *IEEE Trans. Plas. Sci.* 34 (2006): 5.

Kantsyrev, V. L., Safronova, A. S., Esaulov, A. A., Williamson, K. M., Shrestha, I., Yilmaz, F., Osborne, G. C., Weller, M. E., Ouart, N. D., Shlyaptseva, V. V., Rudakov, L. I., Chuvatin, A. S., Velikovich, A. L. "A review of new wire arrays with open and closed magnetic configurations at the 1.6 MA Zebra Generator." *High Energy Density Phys.* 5 (2009): 115-123.

Kantsyrev, V. L.; Safronova, A. S.; Esaulov, A. A.; Williamson, K. M.; Shrestha, I.; Osborne, G. C.; Weller, M. E.; Yilmaz, M. F.; Ouart, N. D.; Shlyaptseva, V. V.; Velikovich, A. L.; Rudakov, L. I. "X-ray pulse shaping in experiments with planar wire arrays at the 1.6 MA Zebra generator." *Journal of Phys.* 244 (2010): 032030.

Lebedev, S. V.; Beg, F. N.; Bland, S. N.; Chittenden, J. P.; Dangor, A. E.; Haines, M. G. "Snowplow-like behavior in the implosion phase of wire array Z pinches." *Phys. of Plasmas* 9 (2002): 2293

Mikolajczyk, J., Blelecki, Z., Nowakowski, M., Wojtas, J. "Investigation of Detector Responsivity in the 'Water Window' Wavelength Range." *PIERS Proceedings* (2010).

Nave, R. "Circular Aperture Diffraction." HyperPhysics. (2005). Web. 2013.

Nishio, M., Shrestha, I., Kantsyrev, V. L., Tooth, M., Takasugi, T. "Note: Application of UF-4 emulsion films to detect low-energy ions produced by laser ablation plasma." Manuscript submitted for publication. (2013).

Ouart, N. D. "Radiative properties of Z-pinch and laser produced plasmas from mid-atomic-number materials." Diss. University of Nevada, Reno, 2010. Print.

Safronova, A.S.; Hansen, S. B., Kantsyrev, V. L., Fedin, D. A., Ouart, N., Fournier, K. B., Safronova, U. I. "Advanced spectroscopic analysis of 0.8—1.0-MA Mo x pinches and the influence of plasma electron beams on L-shell spectra of Mo ions." *Phys. Rev. E* 67 (2003): 026409-1.

Safronova, A. S., Kantsyrev, V. L., Ouart, N., Yilmaz, F., Fedin, D., Astanovitsky, A., LeGalloudec, B., Batie, S., Brown, D., Nalajala, V., Pokala, S., Shrestha, I., Cowan, T. E., Jones, B., Coverdale, C. A., Deeney, C., Hansen, S.B., LePell, P.D., Jobe, D., Nielson, D. "Spectroscopic modeling of radiation from Cu and Mo X-pinch produced on the UNR 1 MA Zebra generator." *Journal of Quantitative Spectroscopy and Radiative Transfer* 99 (2006): 560-571.

Safronova, A. S., Esaulov, A. A., Kantsyrev, V. L., Ouart, N. D., Shlyaptseva, V., Weller, M. E., Keim, S. F., Williamson, K. M., Shrestha, I., Osborne, G. C. "Searching for efficient X-ray radiators for wire array Z-pinch plasmas using mid-atomic-number single planar wire arrays on Zebra at UNR." *High Energy Density Phys.* 7 (2011): 252-258.

Scudder, D. W.; Schlachter, J. S.; Hammel, J. E.; Venneri, F.; Chrien, R.; Lovberg, R.; Riley, R. "The Los Alamos megamp fiber z-pinch experiment. Phys. of Alt. Magnetic Confinement Schemes" *Prof. SIF* (1991): 519-525.

Shelkovenko, T.A.; Sinars, D. B., Pikuz, S. A., Hammer, D. A. "Radiographic and spectroscopic studies of X-pinch plasma implosion dynamics and x-ray burst emission characteristics." *Phys. Plasmas* 8(4) (2001): 1305-1318.

Shlyaptseva, A. S., Hansen, S. B., Kantsyrev, V. L., Bauer, B., Fedin, D. A., Ouart, N. D., Keely, S., LeBeau, H., Safronova, U. I. "X-ray spectropolarimetry of high-temperature plasmas." *Rev. Sci. Instr.* 72(1) (2001): 1241-1244.

Sinars, D. B.; Hu, M.; Chandler, K. M.; Shelkovenko, T. A.; Pikuz, S. A.; Greenly, J. B.; Hammer, D. A.; Kusse, B. R. "Experiments measuring the initial energy deposition, expansion rates and morphology of exploding wires with about 1 kA/wire." *Phys. of Plasmas* 8 (2001): 216.

Sinars, D. B., McBride, R. D., Pikuz, S. A., Shelkovenko, T. A., Wenger, D. F., Cuneo, M. E., Yu, E. P., Chittenden, J. P., Harding, E. C., Hansen, S. B., Peyton, B. P., Ampleford, D. J., Jennings, C. A. "Investigation of High-Temperature Bright Plasma X-ray Sources Produced in 5-MA X-Pinch Experiments." *Physical Review Letters* 109(15) (2012): 15502(5).

Spielman, R. B. "Diamond photoconducting detectors as high power z-pinch diagnostics." *Rev. Sci. Instr.* 66 (1995): 867.

Weller, M. E., Safronova, A. S., Clementson, J., Kantsyrev, V. L., Safronova, U. I., Beiersdorfer, P., Petkov, E. E., Wilcox, P. G., Osborne, G. C. (2012). "Extreme ultraviolet spectroscopy and modeling of Cu on the SSPX Spheromak and laser plasma 'Sparky'." *Review of Scientific Instruments* 83 (2012): 10E101(3).

Williamson, K. M. "Implosion and Radiation Dynamics of Cylindrical and Planar Wire Array Z-pinch Plasma." Diss. University of Nevada, Reno, 2011. Print.

Zakharov, S. M., G.V. Ivanenkov, A.A. Kolomenskii, S.A. Pikuz, A.I. Samokhin and I. Ulshmid. "Wire x pinch in high current diode." *Sov. Tech. Phys. Lett.* 8(9) (1982): 456.

Zakharov, S. M., G.V. Ivanenkov, A.A. Kolomenskii, S.A. Pikuz, A.I. Samokhin. "Study of plasma of exploding multiwire loads in diode of high-current accelerator discharge". *Sov. J. Plasma Phys* 13 (1987): 115-124.